7

Linking ice and gas in the Coronet cluster in Corona Australis

G. Perotti[1], J. K. Jørgensen[1], L. E. Kristensen[1], W. R. M. Rocha[1], E. Artur de la Villarmois[2], H. J. Fraser[3], P. Bjerkeli[4], M. Sewilo[5], S. B. Charnley[5]

[1] Niels Bohr Institute & Centre for Star and Planet Formation, University of Copenhagen, Øster Voldgade 5−7, 1350 Copenhagen K., Denmark
[2] Instituto de Astrofísica, Ponticia Universidad Católica de Chile, Av. Vicuña Mackenna 4860, 7820436 Macul, Santiago, Chile
[3] School of Physical Sciences, The Open University, Walton Hall, Milton Keynes, MK7 6AA, United Kingdom
[4] Department of Space, Earth, and Environment, Chalmers University of Technology, Onsala Space Observatory, 439 92 Onsala, Sweden
[5] NASA Goddard Space Flight Center, 8800 Greenbelt Road, Greenbelt, MD 20771, USA

In preparation

Abstract

Context. The planet-forming material is inherited from the molecular cloud via an infalling protostellar envelope. During its journey from the cloud to the disk, the chemical composition of the protostellar envelope matter is preserved or processed to various degrees based on the surrounding physical environment.

Aims. We constrain the interplay of the gas and ice in the envelopes surrounding protostars in the Coronet cluster in Corona Australis, and assess the importance of irradiation by the nearby Herbig Ae/Be star R CrA.

Methods. We present 1.3 mm Submillimeter Array (SMA) observations towards the envelopes of low-mass protostars (Class I or younger) in the Coronet cluster. Additionally, we make use of archival SMA, APEX and Spitzer IRS observations to analyse the relationships between ice and gas species in this strongly irradiated region. Finally,

we calculate methanol (CH_3OH) gas-to-ice ratios and compare them with ratios determined towards protostars located in Serpens Main and in the λ Orionis Barnard 35A cloud.

Results. In the SMA data we identify eighteen molecular transitions and a total of nine species which include molecular ions, deuterated species, and isotopologues. The high UV flux appears to impact the gas-phase chemistry in the Coronet by enhancing the emission of molecular tracers such as H_2CO, SO, SO_2, and SiO. The distribution of CH_3OH gas-to-ice ratios covers one order of magnitude (1.9×10^{-4} to 1.5×10^{-3}) and validates previous laboratory predictions. The CH_3OH gas-to-ice ratios estimated in different star-forming regions are similar, indicating that the overall CH_3OH chemistry of cold low-mass envelopes is relatively independent of variations in the physical conditions. A larger sample is however required to constrain further this result and the impact of the environment on the physico-chemical evolution of protostellar envelope material.

7.1 INTRODUCTION

Sun-type stars and planets form inside molecular clouds, when dense cores undergo gravitational collapse. While collapsing, the gas and dust constituting the clouds is assembled into infalling envelopes, streamers and circumstellar disks, which supply the fundamental ingredients for planet formation. Recent observations (e.g., Andrews *et al.*, 2018; Keppler *et al.*, 2018; Segura-Cox *et al.*, 2020) suggest that planets form earlier than previously thought (a few $\times10^5$yr; Tychoniec *et al.*, 2020) and in tandem with their host star (Alves *et al.*, 2020). In this context, it is still unclear whether the cloud material is preserved when becoming part of planets or, instead, entirely thermally processed losing the cloud chemical fingerprint (see reviews, e.g., Jørgensen *et al.*, 2020; Öberg and Bergin, 2021; van Dishoeck and Bergin, 2020). If the planet-building material is preserved, a key question yet to be answered is to what extent the composition of the gas and ice material is altered during its journey from the cloud to the disk.

To address this query it is necessary to study how the environment impacts the physical and chemical properties of embedded protostars and disks. For instance, external irradiation (Winter *et al.*, 2020) and cosmic ray ionization (Kuffmeier *et al.*, 2020) might shape the chemical and physical evolution of forming low-mass stars by e.g., photoevaporating their disks (van Terwisga *et al.*, 2020; Haworth *et al.*, 2021 and references therein) or leading to less massive disks (Cazzoletti *et al.*, 2019). In this chapter we investigate the variations of the gas and ice composition towards deeply embedded sources in Corona Australis, to study the effects of external irradiation on the gas-to-ice ratios.

Corona Australis (CrA) is one of the nearest regions with ongoing star-formation, located at a distance of 149.4±0.4 pc as estimated from *Gaia*-DR2 measurements (Galli *et al.*, 2020). The most updated census of the cloud counts 262 young stellar object (YSO) candidates, mostly Class II or III, predominantly concentrated in the most extincted region, the "head"

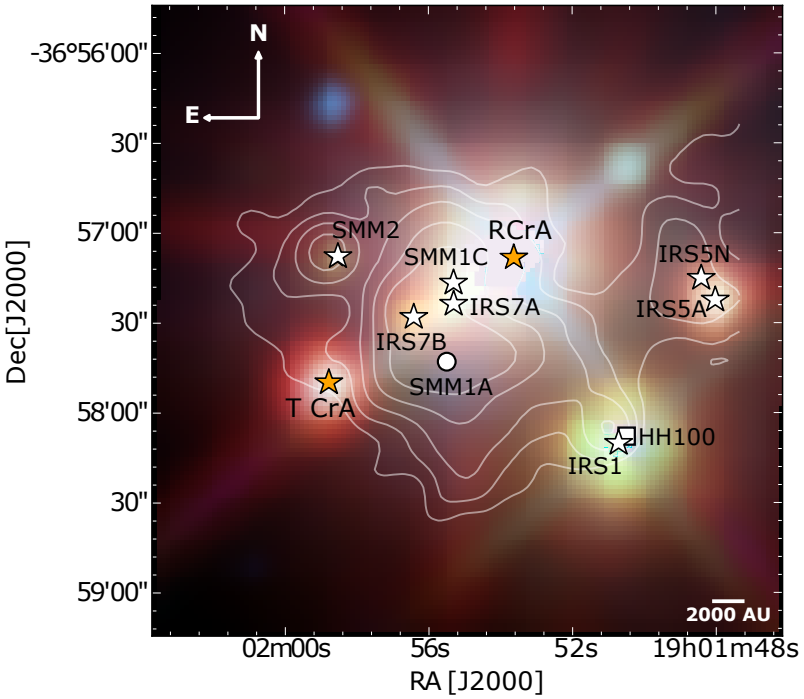

FIGURE 7.1.1: Three-color image of the Coronet cluster overlaid with SCUBA 850 μm density flux (Nutter *et al.*, 2005); contours are in decreasing steps starting at the peak flux (3.7 Jy beam^{-1}) and subtracting 30% from the previous level. The composite is made from *WISE* 3.4 μm (blue), 4.6 μm (green) and 12 μm (red) bands (Wright *et al.*, 2010). The white stars mark the positions of Class 0/I YSOs in the R CrA/Coronet region (Peterson *et al.*, 2011; Nutter *et al.*, 2005), whereas the orange stars indicate the Herbig Ae/Be star R CrA and the T Tauri star T CrA. The pre-stellar core candidate SMM1A is indicated with a white circle and the white square represents the Herbig Haro object HH100. These symbols will be adopted throughout the chapter.

(Peterson *et al.*, 2011; Alves *et al.*, 2014). The correlation between the star formation activity and the head-tail structure of Corona Australis has been investigated by Dib and Henning (2019), who found that the spatial distribution of dense cores is a consequence of the physical conditions of the large scale environment present at the time the cloud assembled. The youngest population of YSO (Class 0/I) is situated in the Coronet cluster (Taylor and Storey, 1984; Forbrich *et al.*, 2007; Forbrich and Preibisch, 2007), also associated with the luminous Herbig Ae/Be star R CrA (Peterson *et al.*, 2011).

Figure 7.1.1 displays a section of the Coronet cluster and a summary of the principal cluster members is provided in Table 7.1.1. The Herbig Ae/Be R CrA (spectral type B5–B8; Gray *et al.*, 2006; Bibo *et al.*, 1992) is the brightest star in this very young cluster. Due to its variable nature (Herbig, 1960), its stellar mass and luminosity are uncertain (Mesa *et al.*, 2019). Recent *Very Large Telescope*/SPHERE observations of R CrA resolved a companion at a separation of ~0.156″–0.184″ and complex extended jet-like structures around the star (Mesa *et al.*, 2019). A second variable star, the T Tauri star T CrA is present in the Coronet cluster, approximately 30″ to the south-east of R CrA (Herbig, 1960; Taylor and Storey, 1984). The region between the two variable stars harbours a wealth of Class 0/I YSOs (Table 7.1.1).

The Coronet cluster members have been at the center of active multi-

TABLE 7.1.1: Overview of the Coronet cluster objects.

Object	RA [J2000]	DEC [J2000]	Designation[a]	Other names[b]
IRS5A	19:01:48.03	-36:57:22.2	Class I YSO	CrA-19
IRS5N	19:01:48.46	-36:57:14.7	Class I YSO	CrA-20
HH100 IRS1	19:01:50.56	-36:58:08.9	Herbig-Haro object	–
IRS1	19:01:50.68	-36:58:09.7	Class I YSO	VSSt 15, TS 2.6
R CrA	19:01:53.67	-36:57:08.0	Herbig Ae/Be star	–
SMM1C	19:01:55.29	-36:57:17.0	Class I YSO	B9, Brown 9
IRS7A	19:01:55.32	-36:57:21.9	Class I YSO	IRS7W, IRS7
SMM1A	19:01:55.60	-36:57:43.0	Pre-stellar core	–
IRS7B	19:01:56.40	-36:57:28.3	Class I YSO	SMM1B, IRS7E
SMM2	19:01:58.54	-36:57:08.5	Class I YSO	CrA-43, WMB55
T CrA	19:01:58.78	-36:57:49.9	T Tauri star	–

Notes. All the coordinates are taken from Peterson *et al.* (2011), except for SMM1A which comes from Nutter *et al.* (2005) and HH100 IRS1 from Boogert *et al.* (2008). [a] The YSO class is assigned from the spectral index α reported in Peterson *et al.* (2011); the objects designated as "Class I YSO" are Class I or younger. [b] From Peterson *et al.* (2011) and Lindberg and Jørgensen (2012).

wavelength research, mostly aimed at the characterization of the properties of YSOs at very early stages of stellar evolution. Some of the most studied objects are IRS7B and IRS7A, identified with the *Very Large Array* at 6 cm by Brown (1987). (Sub)millimeter studies detected three additional continuum point sources in the region: SMM1A, SMM1C, and SMM2 (Nutter *et al.*, 2005; Groppi *et al.*, 2007; Miettinen *et al.*, 2008; Chen and Arce, 2010; Peterson *et al.*, 2011). The spectral energy distributions (SEDs) of the cluster members have been investigated by Groppi *et al.* (2007), suggesting that SMM1C is a Class 0 YSO and IRS7B is a transitional Class 0/I object. IRS7A and SMM2 are likely Class I sources (Peterson *et al.*, 2011) and SMM1A is classified as a pre-stellar core candidate (Nutter *et al.*, 2005; Chen and Arce, 2010). IRS1, IRS5N and IRS5A are suggested as Class I YSO based on submillimeter and infrared observations (Peterson *et al.*, 2011).

Along with the identification and the age estimation of the YSOs in the Coronet, their chemical evolution has been monitored in the past decades. The line-rich spectra of IRS7B and IRS7A has been investigated using the *Atacama Pathfinder EXperiment* (APEX) single-dish telescope by Schöier *et al.* (2006), who reported diverging kinetic temperatures for formaldehyde and methanol (>30 K for H_2CO and ≈20 K for CH_3OH). Lindberg and Jørgensen (2012) suggested that the high temperatures in the region (>30 K) traced by the emission of formaldehyde, are caused by external irradiation from the Herbig Ae/Be star R CrA. With the purpose of analyzing the impact of external irradiation on the molecular inventory of low-mass protostars, systematic unbiased line surveys have been carried out firstly towards IRS7B using the *Atacama Submillimeter Telescope Experiment* (ASTE) by Watanabe *et al.* (2012), and extended to other Coronet cluster members using APEX by Lindberg *et al.* (2015).

These systematic surveys confirmed that external irradiation can affect the chemical nature of protostars, particularly by enhancing the abundances of Photon-Dominated Regions (PDRs) tracers (Watanabe *et al.*, 2012; Lindberg and Jørgensen, 2012). High-resolution *Atacama Large Millimeter/submillimeter Array* (ALMA) observations towards IR7B by Lindberg *et al.* (2014) revealed a possible additional effect of external irradiation on the chemistry of protostars: the low abundance of complex organic molecules such as CH_3OH in the inner hot regions of protostellar envelopes (<100 AU). However, the authors also suggest that the faint CH_3OH emission might be due to a flat density profile of the inner envelope due to the presence of a disc.

The composition of interstellar ices towards a few objects in Corona Australis (IRS5A, IRS5B, HH100 IRS1, IRS7A, IRS7B, IRAS32) has been investigated in the near-infrared (3−5 μm) with the *Very Large Telescope* (VLT; Pontoppidan *et al.*, 2003a), in the mid-infrared (5−8 μm) using the *Infrared Space Observatory* (ISO; Keane *et al.*, 2001) and as part of the *Spitzer* c2d Legacy Program (5−8 μm by Boogert *et al.*, 2008; 8−10 μm by Bottinelli *et al.*, 2010, and 14.5−16.5 μm by Pontoppidan *et al.*, 2008). Ice features attributed to H_2O, CO, CO_2, NH_3, CH_3OH were securely identified in the astronomical spectra of the targeted sources. Upper limits on formic acid (HCOOH) and abundances of ammonium ion (NH_4^+) relative to H_2O ice were presented by Boogert *et al.* (2008), with the caveat that the feature at 6.85 μm has not been unequivocally attributed to NH_4^+.

This chapter explores the variations of the gas and ice composition in the Coronet, investigating the effects of external irradiation on the intertwined gas-phase and solid-state chemistries of the youngest objects in the Corona Australis star-forming region. We present SMA observations towards five Coronet cluster members, complementing previous SMA observations by Lindberg and Jørgensen (2012) at 1.3 mm, thus increasing the number of detected chemical species towards the YSOs lying in this region. Furthermore, the dependencies of gas-to-ice ratios on the physical conditions are addressed, by determining gas-to-ice ratios of CH_3OH in this strongly irradiated cluster and comparing them with ratios obtained towards less irradiated low-mass star-forming regions.

The chapter is organized is as follows. We begin in Section 7.2 by describing the observational setups, the data reduction strategy and the ancillary data to the SMA observations. In Section 7.3 we present our key observational results, while the variations on the ice and gas composition are analysed in Section 7.4. Section 7.5 discusses the determined CH_3OH gas-to-ice ratios and Section 7.6 summarises our conclusions and lists avenues for future studies.

7.2 OBSERVATIONS AND ARCHIVAL DATA

7.2.1 *SMA observations*

The Coronet cluster was observed with the *Submillimeter Array* (SMA; Ho *et al.*, 2004) on February 25, 2020 using 7 antennas in the compact configuration. The region was covered by one pointing ~ 10″ south of

R CrA (Fig. 7.3.1) with coordinates α_{J2000} = $19^{h}01^{m}53^{s}.30$, δ_{J2000} = −36°57′21.″00. The SWARM correlator provided a total frequency coverage of 16 GHz, with the lower sideband covering frequencies from 213.3 to 221.3 GHz and upper sideband 229.3 to 237.3 GHz. The spectral resolution was 0.6 MHz corresponding to 0.7 km s^{-1}.

[1] http://casa.nrao.edu/

Data calibration and imaging were performed with the CASA package[1] (McMullin *et al.*, 2007). The complex gains were calibrated through observations of the quasars 1924-292 and 1957-387 and the bandpass through observations of the bright quasar 3c279. The overall flux calibration was done through observations of Callisto. Imaging was done using the `tclean` algorithm and a Briggs weighting with robustness parameter of 1. The resulting synthetic beam size of the SMA observations was 4.″9 × 2.″6 with a position angle of -8.2°.

7.2.2 *Ancillary data*

This study made use of ancillary data to the SMA observations, primarily to compare the gas and ice molecular inventory in the Coronet. Ice column densities were adopted from *Spitzer* InfraRed Spectrograph (IRS) observations presented by Boogert *et al.* (2008) and the H_2CO and CH_3OH gas-phase column densities were taken from Lindberg and Jørgensen (2012) and Lindberg *et al.* (2015). A map of the H_2 column density towards the R CrA region was constructed using submillimeter continuum maps at 850 μm obtained with the SCUBA camera at the *James Clerk Maxwell Telescope* (JCMT; Nutter *et al.*, 2005). The H_2 column density map was used in the calculation of the abundances of the gas-phase and ice species.

7.3 RESULTS

7.3.1 *Gas-phase detections*

Figure 7.3.1 displays the SMA 1.3 mm continuum emission towards the Coronet cluster. The morphology of the continuum coincides with the position of the targeted young stellar objects in the region. The faint emission of one of the condensations associated with the pre-stellar core candidate SMM1A, SMM1A-c, is also seen (Chen and Arce, 2010). The peak emission is observed towards the two Class 0 sources SMM1C and IRS7B, followed by the Class I object IRS7A and the Herbig Ae/Be star R CrA.

Eighteen molecular transitions and a total of nine species were identified in the SMA data set, in two 8 GHz frequency ranges (213.3−221.3 GHz and 229.3−237.3 GHz). The detected inventory includes molecular ions, deuterated species and isotopologues: CO (^{13}CO and $C^{18}O$), H_2CO (D_2CO), CH_3OH, DCO^+, SO, SO_2, c-C_3H_2, HC_3N, SiO (Table 7.3.1). The line emission is predominantly extended and it does not necessarily coincide with the position of the compact continuum sources in the Coronet cluster (Figures 7.3.1 −7.3.4). In contrast, it is mostly localized to the east of the Herbig Ae/Be star R CrA and to the south of the young stellar objects IRS7A and IRS7B, at the pre-stellar core SMM1A position. This statement applies especially to H_2CO and CH_3OH, and is consistent with previous 1.3 mm SMA observations of the region by Lindberg and Jørgensen (2012) covering frequencies in the

TABLE 7.3.1: Identified molecular transitions in the SMA data.

Species	Transition	Frequency[a] [GHz]	$A^a_{\rm ul}$ [s^{-1}]	$E^a_{\rm u}$ [K]
CO-species				
CO	$J = 2 - 1$	230.538	6.92×10^{-7}	17
$C^{18}O$	$J = 2 - 1$	219.560	6.01×10^{-7}	16
^{13}CO	$J = 2 - 1$	220.398	6.04×10^{-7}	16
H_2CO	$3_{0,3} - 2_{0,2}$	218.222	2.82×10^{-4}	21
H_2CO	$3_{2,2} - 2_{2,1}$	218.476	1.58×10^{-4}	68
H_2CO	$3_{2,1} - 2_{2,0}$	218.760	1.58×10^{-4}	68
CH_3OH	$4_2 - 3_1$, E	218.440	4.68×10^{-5}	46
CH_3OH	$8_{-1} - 7_0$, E	229.758	4.19×10^{-5}	89
Deuterated-species				
D_2CO	$4_{0,4} - 3_{0,3}$	231.410	3.47×10^{-4}	28
DCO^+	$J = 3 - 2$	216.112	2.57×10^{-4}	21
S-species				
SO	$5_5 - 4_4$	215.220	1.20×10^{-4}	44
SO	$6_5 - 5_4$	219.949	1.35×10^{-4}	35
SO_2	$4_{2,2} - 3_{1,3}$	235.151	7.69×10^{-5}	19
Carbon-chain species				
c-C_3H_2	$3_{3,0} - 2_{2,1}$	216.278	2.57×10^{-4}	19
c-C_3H_2	$6_{0,6} - 5_{1,5}$	217.822	5.37×10^{-4}	39
c-C_3H_2	$5_{1,4} - 4_{2,3}$	217.940	3.98×10^{-4}	35
HC_3N	$J = 24 - 23$	218.324	8.32×10^{-4}	131
Other species				
SiO	$J = 5 - 4$	217.104	5.25×10^{-4}	31

Notes.[a] From the Cologne Database for Molecular Spectroscopy (CDMS; Müller *et al.*, 2001) and the Jet Propulsion Laboratory catalog (Pickett *et al.*, 1998).

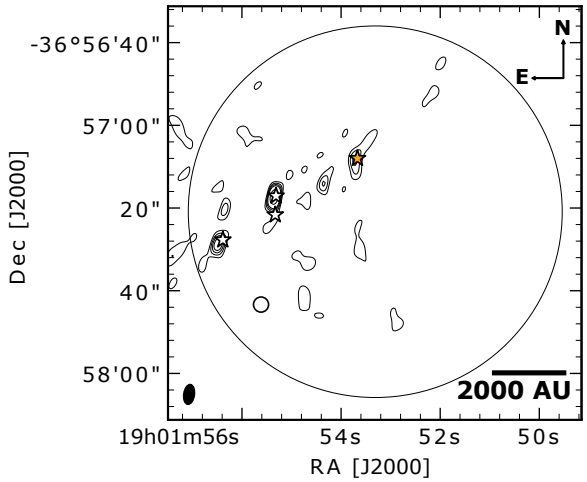

FIGURE 7.3.1: SMA continuum at 1.3 mm. The contours are at 3σ, 6σ, 9σ, 12σ, and continue in steps of 10σ (σ = 4.3 mJy). The circle indicates the SMA primary beam size, whereas the synthetic beam is represented with a black ellipse in the bottom left corner. The stars mark the position of the objects located in the Coronet cluster, refer to Fig. 7.1.1 for their identification.

ranges 216.849–218.831 GHz and 226.849–228.831 GHz. In contrast, no line emission was detected towards SMM1A in the SMA data set presented by Chen and Arce (2010), although the SMA correlator covered the same spectral ranges analysed by Lindberg and Jørgensen (2012).

The detected species can be divided into four groups based on their distribution (Table 7.3.1): (I) CO species, (II) S-species, (III) carbon-chain species, and (IV) SiO. The distribution of the emission of the deuterated species does not show peculiar patterns, instead it presents common features to the CO-species and therefore it will be discussed with group (I). A list of non-detected molecular transitions is given in Appendix 7.A, Table 7.A.1.

CO-species

Figures 7.3.2 and 7.3.3 display integrated intensity maps for CO, ^{13}CO, C^{18}O, H_2CO and its deuterated form (D_2CO), and CH_3OH. The distribution of the CO-species emission is extended, especially for CO and its isotopologues, CH_3OH and D_2CO. The three transitions of H_2CO show the same emission pattern (Figure 7.3.2, panels $d - f$). The emission is localized in two ridges: the northern ridge between R CrA and SMM1C, and the southern ridge to the south of IRS7B, at the SMM1A position. No bright line emission is observed towards the young stellar objects SMM1C, IRS7A,and IRS7B. The emission offset from the YSOs positions and the elongated shape of the ridges are indicators of external heating. The emission localized in the southern ridge traces the three condensations within the pre-stellar core SMM1A (SMM1A-a, SMM1A-b, and SMM1A-c), observed in the SMA dust continuum by Chen and Arce (2010).

The strength of the H_2CO emission, for the three detected H_2CO lines is comparable in both ridges. A different morphology pattern is observed for the other CO-species, especially for CO, its isotopologues and DCO^+ (Figure 7.3.3, panel j) which do not show bright line emission towards SMM1A, and for CH_3OH, for which the emission peak is located within the SMM1A core and it does not show a northern ridge (Figure 7.3.3, panels

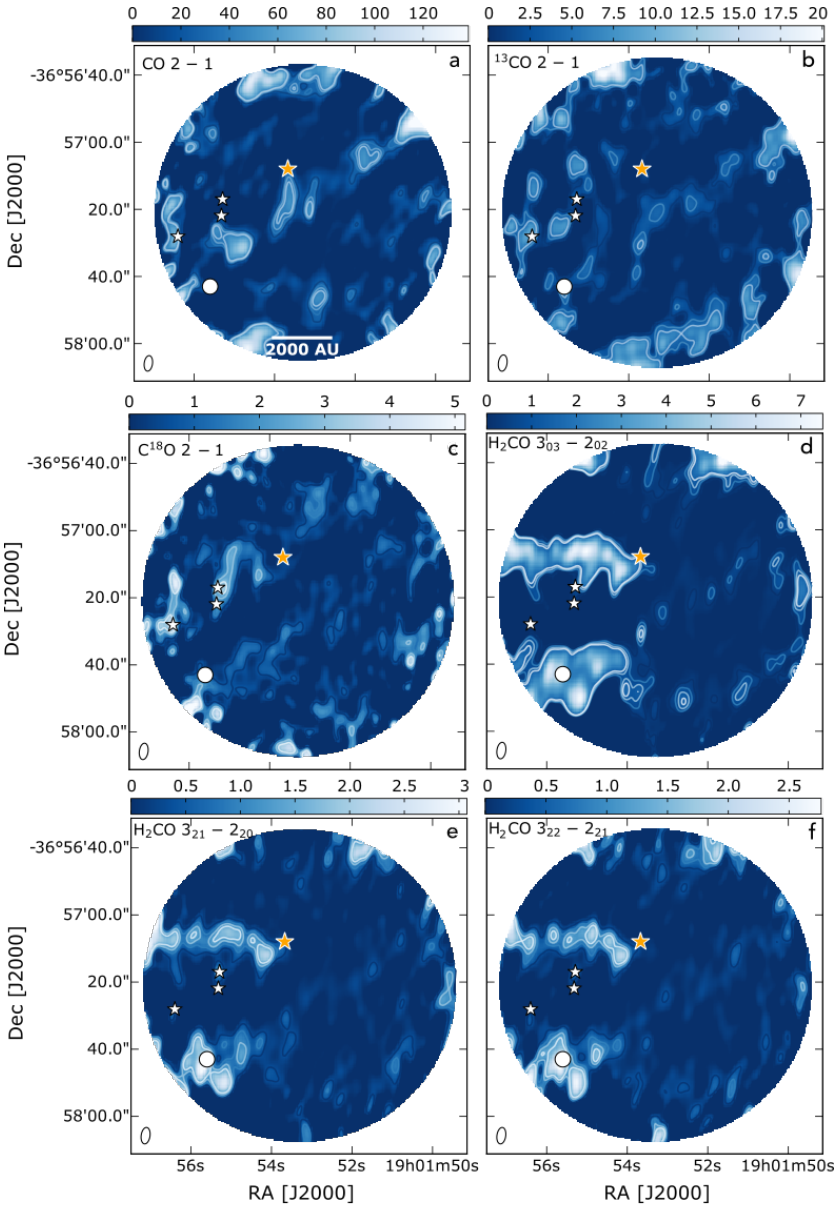

FIGURE 7.3.2: Primary beam corrected Integrated intensity maps for the different species observed with the SMA. In each plot contours start at 5σ and continue in intervals of 5σ. Shown are (a) CO $J = 2 - 1$ ($\sigma = 0.24$ Jy beam^{-1}km s^{-1}), (b) ^{13}CO $J = 2 - 1$ ($\sigma = 0.17$ Jy beam^{-1}km s^{-1}), (b) C^{18}O $J = 2 - 1$ ($\sigma = 0.15$ Jy beam^{-1}km s^{-1}), (d) H$_2$CO 3_{03}–2_{02} ($\sigma =$ 69 mJy beam^{-1}km s^{-1}), (e) H$_2$CO 3_{21}–2_{20} ($\sigma = 71$ mJy beam^{-1}km s^{-1}), (f) H$_2$CO 3_{22}–2_{21} ($\sigma = 65$ mJy beam^{-1}km s^{-1}). The circles outline the SMA primary beam. The synthesized beams are shown in white in the bottom left corner of each panel. The stars and the dots mark the position of the Coronet cluster objects as in Fig. 7.1.1.

$g - h$). In contrast to the other CO-species, the line emission of C^{18}O and DCO$^+$ is also observed at the SMM1C and IRS7B positions (Figures 7.3.2 and 7.3.3, panels c, i, and j).

S-species

The SO and SO$_2$ line emissions appear relatively bright and compact (Figures 7.3.3 and 7.3.4, panels $k - m$), compared to the CO-species. The distribution of the emission is identical for the three transitions, and it peaks towards IRS7A and SMM1C. The strength of the emission among the SO

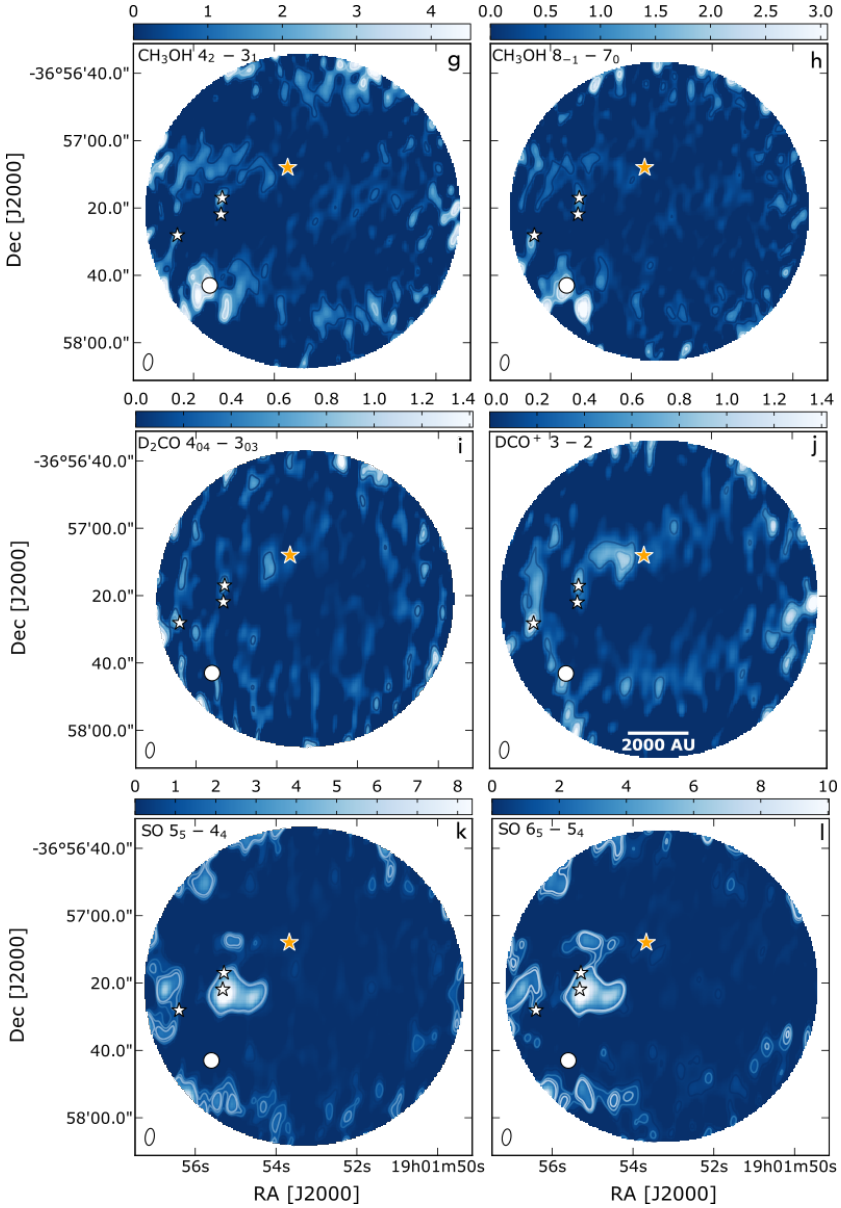

FIGURE 7.3.3: Continued from Figure 7.3.2. Primary beam corrected integrated intensity (Jy beam km s^{-1}) maps for: g) CH_3OH 4_2–3_1 (σ = 0.15 Jy beam^{-1}km s^{-1}), (h) CH_3OH 8_{-1}–7_0 (σ = 88 mJy beam^{-1}km s^{-1}) and (i) D_2CO 4_{04}–3_{03} (σ = 81 mJy beam^{-1}km s^{-1}), (j) DCO^+ J = 3 – 2 (σ = 81 mJy beam^{-1}km s^{-1}), (k) SO 5_5 – 4_4 (σ = 88 mJy beam^{-1}km s^{-1}), (l) SO 6_5 – 5_4 (σ = 95 mJy beam^{-1}km s^{-1}) detected with the SMA.

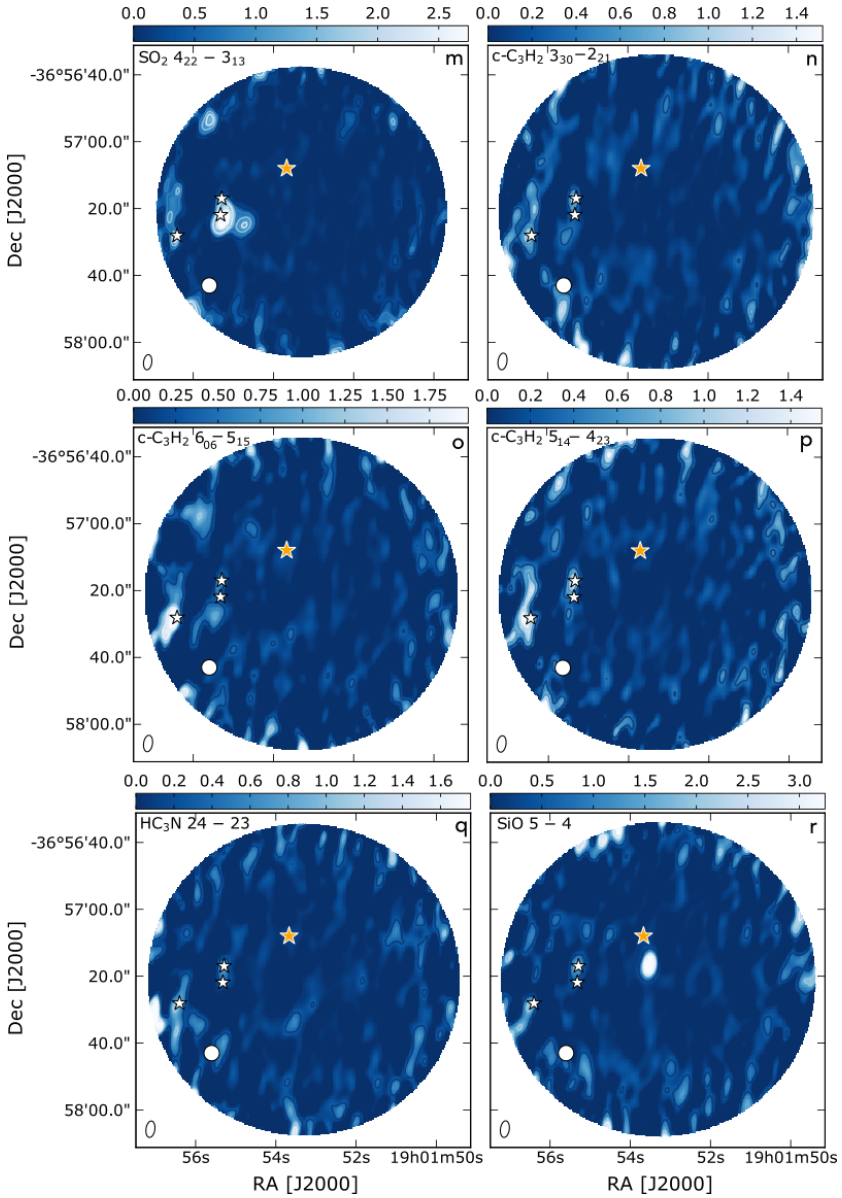

FIGURE 7.3.4: Continued from Figure 7.3.3. Primary beam corrected integrated intensity (Jy beam km s^{-1}) maps for: (m) SO_2 $4_{22}-3_{13}$ (σ = 61 mJy beam^{-1}km s^{-1}), (n) c-C_3H_2 3_{30}–2_{21} (σ = 76 mJy beam^{-1}km s^{-1}), (o) c-C_3H_2 6_{06}–5_{15} (σ = 74 mJy beam^{-1}km s^{-1}), (p) c-C_3H_2 5_{14}–4_{23} (σ = 85 mJy beam^{-1}km s^{-1}), (q) HC_3N J = 24 – 23 (σ = 64 mJy beam^{-1}km s^{-1}) and (r) SiO J = 5 – 4 (σ = 0.12 mJy beam^{-1}km s^{-1}) detected with the SMA.

transitions is similar (7–10 Jy beam km s^{-1}; Figure 7.3.3, panels $k - l$). The SO_2 emission is approximately a factor of four lower (Figure 7.3.4, panels m). SO and SO_2 are molecular tracers of energetic inputs in the form of outflows and jets. The luminous SO and SO_2 emissions indicate that high-velocity flows of matter are present in the field-of-view of the observations, associated with IRS7A and SMM1C. This result is in agreement with studies of the Herbig-Haro objects in the Coronet attributed to SMM1C (Wang *et al.*, 2004; Peterson *et al.*, 2011).

Carbon-chain species

The third group of lines corresponds to carbon-chain species like c-C_3H_2 and HC_3N which show a fairly weak emission (1.4–1.75 Jy beam km s^{-1}) compared to the previous two groups (CO- and S-species). Their emission is diffuse and characterized by a fairly low S/N. In contrast to the majority of the CO-species, the carbon-chain and the S-species have their strongest emission associated with the YSOs position: for instance the the c-C_3H_2 transitions peak at the IRS7B location (Figure 7.3.4, panels o, p).

SiO

The SiO emission shows an interesting and distinct feature compared to the other three groups (Figure 7.3.4, panel r), as it appears as a bright point source just south of R CrA, to the west of SMM1C and IRS7A at velocities remarkably higher (9–12 km s^{-1}) than the R CrA velocity (5 km s^{-1}). The emission is aligned with R CrA. The same compact structure for the SiO emission has been observed previously by Lindberg and Jørgensen (2012), who concluded that it might be associated with Herbig-Haro (HH) objects in the Coronet. This result is based on observations of multiple HH objects extending south of R CrA coinciding with the location of the SiO emission detected in the SMA data. It has been suggested that HH objects in the region are emanated from the infrared source IRS1 (e.g., HH100, HH101; Hartigan and Graham, 1987), however, more recent studies (Wang *et al.*, 2004; Peterson *et al.*, 2011) infer that both R CrA and SMM1C could be plausible driving sources.

In general, the emission reported in the SMA data sets is dominated by molecular tracers such as H_2CO SO, SO_2, SiO. The enhanced emission of H_2CO is consistent with temperature variations in the field of view of the observations, and particularly with the external irradiation from the variable stars in the region (R CrA and T CrA). In contrast, the shock tracers (SO, SO_2, SiO) probe the numerous outflows and Herbig-Haro objects in the region, which are indicators of a young stellar population in the earliest evolutionary stages.

TABLE 7.3.2: Total ice and gas column densities towards the Coronet cluster members.

Object	$N^{ice}_{H_2O}$	$N^{ice}_{CH_3OH}$	$N^{ice}_{NH_4^+}$	$^{\dagger}N^{gas}_{H_2CO}$	$^{\dagger}N^{gas}_{CH_3OH}$	$N^{SCUBA}_{H_2}$
	$[10^{18}cm^{-2}]$	$[10^{17}cm^{-2}]$	$[10^{17}cm^{-2}]$	$[10^{13}cm^{-2}]$	$[10^{13}cm^{-2}]$	$[10^{23}cm^{-2}]$
IRS5A	3.58 ± 0.26	2.36 ± 0.57	1.83 ± 0.14	3.7±0.74	4.5 ± 2.1	$0.55^{+0.44}_{-0.26}$
HH100 IRS1*	2.45 ± 0.24	< 2.38	2.84 ± 0.51	2.8±0.56	6.7 ± 2.6	$0.67^{+0.51}_{-0.31}$
IRS7A	10.89 ± 1.92	< 4.14	7.62 ± 0.44	4.1±0.82	64 ± 30	$1.48^{+1.12}_{-0.69}$
IRS7B	11.01 ± 1.97	7.49 ± 0.33	6.39 ± 0.22	10±1.0	45 ± 10	$1.92^{+1.45}_{-0.90}$

Notes. Columns 2–4 list the ice column densities from Boogert *et al.* (2008), and assume that NH_4^+ is the carrier of the 6.85 μm feature. † Columns 5 and 6 display the gas column densities from Lindberg and Jørgensen (2012) and Lindberg *et al.* (2015). * The single-dish observations are unable to resolve the emission towards IRS1 and HH100, the value obtained towards IRS1 is adopted here. Columns 7 shows the H_2 column densities using T_{dust}= 30 K. The values in the superscripts and subscripts represent the upper and lower limits if T_{dust}= 20 K or T_{dust}= 50 K are adopted.

7.4 ANALYSIS

In this section, the gas and ice species detected towards the Coronet cluster members are analysed. The ice column densities of H_2O, NH_4^+ and CH_3OH adopted in this chapter were determined by Boogert *et al.* (2008) from *Spitzer* IRS mid-infrared spectra (5–20 μm) as part of the *Spitzer* Legacy Program "From Molecular Cores to Planet-Forming Disks" (c2d). Infrared spectra of IRS5A, HH100 IRS1, IRS7A, and IRS7B were decomposed.

For the gas-phase counterpart, we made use of H_2CO and CH_3OH gas column densities from the combination of Submillimeter Array and APEX 1.3 mm observations by Lindberg and Jørgensen (2012) and Lindberg *et al.* (2015). The adopted ice and gas column densities are reported in Table 7.3.2.

7.4.1 *H_2 column densities*

Prior to searching for gas-ice correlations, the physical structure of the Coronet cluster is investigated by producing an H_2 column density map of the targeted region. This step is required as relative abundances instead of absolute column densities need to be compared when studying gas-ice variations. This is due to the fact that gas and ice observations, by their very nature, are tracing different spatial scales (e.g., Noble *et al.*, 2017), therefore, a comparison between absolute values can lead to misinterpretations.

Figure 7.4.1 shows the H_2 column density map of the Coronet cluster obtained by making use of submillimeter continuum maps at 850 μm (SCUBA; Nutter *et al.*, 2005). A detailed description of the formalism adopted to obtain the H_2 column density from SCUBA maps is provided in Appendix C of Chapter 5. Briefly, in an optically thin thermal dust emission regime, the strength of the submillimeter radiation depends on the column density (N), the dust temperature (T) and the opacity (κ_ν) (Kauffmann *et al.*, 2008). The inserted value for the opacity per unit dust+gas mass is 0.0182 cm^2 g^{-1} ("OH5 dust"; Ossenkopf and Henning, 1994). The adopted values for the dust temperatures are 20, 30, and 50 K, based on previous observational studies and radiative transfer models by Lindberg and Jørgensen (2012) and Lindberg *et al.* (2015).

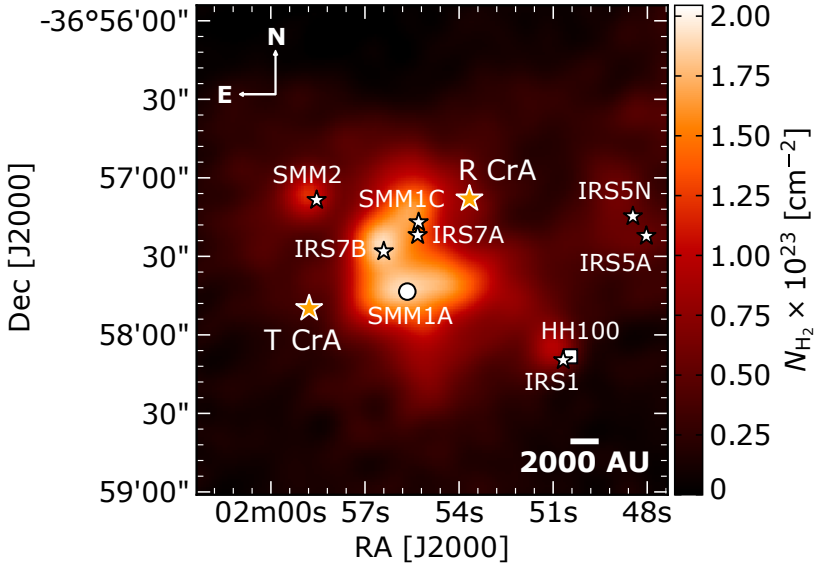

FIGURE 7.4.1: H_2 column density map of the R CrA region calculated from SCUBA dust emission maps at 850 μm (Nutter *et al.*, 2005). Refer to Fig. 7.1.1 for a guide to the symbols of the Coronet cluster objects.

TABLE 7.4.1: Ice and gas abundances relative to H_2 towards the Coronet cluster objects.

Object	$X^{ice}_{H_2O}$	$X^{ice}_{CH_3OH}$	$^*X^{ice}_{NH_4^+}$	$X^{gas}_{H_2CO}$	$X^{gas}_{CH_3OH}$
	[10^{-5}]	[10^{-6}]	[10^{-6}]	[10^{-10}]	[10^{-9}]
IRS5A	6.51 ± 0.51	4.29 ± 1.04	3.33 ± 0.27	6.73 ± 1.36	0.82 ± 0.38
HH100 IRS1	3.66 ± 0.37	< 3.55	4.24 ± 0.77	4.18 ± 0.85	1.0 ± 0.39
IRS7A	7.36 ± 1.32	< 2.98	5.15 ± 0.34	2.77 ± 0.56	4.32 ± 2.03
IRS7B	5.73 ± 1.04	3.90 ± 0.19	3.33 ± 0.15	5.21 ± 0.54	2.34 ± 0.53

Notes. The abundances are relative to $N^{SCUBA}_{H_2}$ (Table 7.3.2). * Assuming that NH_4^+ is the carrier of the 6.85 μm feature (Boogert *et al.*, 2008).

The youngest cluster members are all situated in the densest areas of the targeted region (Fig. 7.4.1); offsets from the dust continuum emission peaks are not observed. The apex of the estimated H_2 column density lies to the south-east of R CrA, and in particular at the IRS7B, SMM1A, SMM1C, and IRS7A positions ($N_{H_2} > 1.45{\times}10^{23}$ cm^{-2}). SMM2, IRS1, IRS5N, and IRS5A are located in slightly less dense regions ($0.5{\times}10^{23}$ cm^{-2} < N_{H_2} < $1.25{\times}10^{23}$ cm^{-2}). The exact values of the H_2 column density are reported in Table 7.3.2.

7.4.2 *Gas and ice variations in the Coronet*

The analysis of the gas-ice variations in the Coronet is addressed in Fig. 7.4.2 by comparing ice and gas fractional abundances (X) relative to H_2 (Table 7.4.1). Panels (a)−(c) report the H_2CO gas abundances as function of H_2O (a), CH_3OH (b), and NH_4^+ (c) ice abundances, whereas panels (d)−(f) display CH_3OH gas abundances with the abundances of the aforementioned

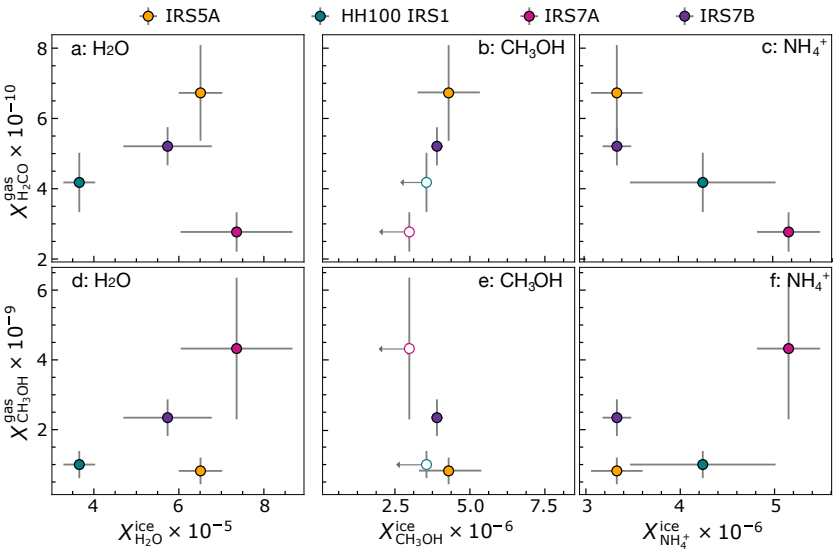

FIGURE 7.4.2: Gas and ice variations in the Coronet cluster. The circles represent the sources listed in Table 7.4.1 for which both gas and ice measurements are available. Panels (a)–(c) display the relations between H_2O, CH_3OH, and NH_4^+ ice and H_2CO gas abundances relative to H_2. Panels (d)–(f) compare H_2O, CH_3OH, and NH_4^+ ice and CH_3OH gas abundances relative to H_2. Upper limits are marked as empty circles.

ice species.

The H_2O ice abundances in Fig. 7.4.2 panels (a) and (d) show the largest spread among all the analysed ice species, with values ranging from 3.7 to 7.4×10^{-5} with respect to H_2 (Table 7.4.1). The lowest H_2O ice abundance is reported towards HH100 IRS1, whereas the highest is found towards IRS7A (Fig. 7.4.2 panel a). The H_2O ice abundances towards IRS5A, IRS7A, and IRS7B are consistent within the uncertainty, only HH100 IRS1 deviates significantly. When H_2O ice and H_2CO gas abundances are compared, no clear correlation is seen. In contrast, a tentative correlation is observed between H_2O ice and CH_3OH gas abundances (Fig. 7.4.2 panel d). IRS5A shows the highest H_2CO gas abundance, whereas IRS7A reports the lowest. The opposite is seen for the CH_3OH gas abundances.

Figure 7.4.2 panels (b) and (e) compare CH_3OH ice abundances versus H_2O and CH_3OH gas abundances. The distribution of the data points in panel (b) hints to a positive trend between CH_3OH ice and H_2CO gas abundances, plausibly indicating a relationship between these two species in the cluster. However, firm conclusions cannot be drawn as the CH_3OH ice abundances towards HH100 IRS1 and IRS7A are upper limits. The same applies to panel (e), where a negative trend is suggested for CH_3OH ice and gas abundances. Finally, Figure 7.4.2 panels (c) and (f) analyse the chemical behaviours of NH_4^+ ice and H_2CO and CH_3OH gas, respectively. The NH_4^+ ice abundances show a minor variation and they are consistent within the error bars. An anti-correlation is observed among the NH_4^+ and H_2CO, indicating that in the regions where H_2CO gas is more abundant (IRS5A and IRS7B), a lower percentage of NH_4^+ resides on the surfaces of the dust grains. In panel (f) no straightforward trend is found among NH_4^+ ice and CH_3OH gas abundances.

The analysis of the gas-ice interplay presented in this section has to be taken with care, as it is based on a small sample. Future high-sensitivity infrared observations will constrain further the abundances of the ice species

and confirm the tentative correlations and anti-correlations observed in Fig. 7.4.2. Additionally, they will allow to carry out statistical studies of the ice variations in the Coronet.

7.4.3 *IRS7A and IRS7B*

Two of the Coronet cluster members for which ice measurements exist are part of the sample observed in this study: IRS7A and IRS7B. It is therefore possible to compare the morphology of the observed emission towards these sources (Figs. 7.3.2 – 7.3.4) with the spatial distribution of the ice species. From Table 7.4.1, the Class I IRS7A reports the highest abundances of H_2O and NH_4^+ compared to the transitional Class 0/I IRS7B. For CH_3OH the comparison is not possible as an upper limit is given for IRS7A.

Among the gas-phase detections reported towards the Coronet, only the emission of the S-bearing and carbon-chain species is compact and localized at the YSOs position. For the S-bearing species, the peak emission is reported towards IRS7A and extends to the west of this source, whereas the emission is faint towards IRS7B. For the carbon-chain species, the situation is reversed. However, the emission of carbon-chain species is weaker and affected by a low-signal to noise. We can conclude that, if the two sources are compared, IRS7A is the source reporting the highest observed emission of S-bearing species and abundance of ice species.

Future observations of the Coronet with the SMA could target the cluster members for which ice data exist. These observations could then be combined to single-dish data to recover the spatially extended emission filtered out by the interferometer, a strategy we adopted previously in Chapters 5 and 6. This will allow to include higher resolution data points for H_2CO and CH_3OH gas abundances in Table 7.4.1 and Figures 7.4.2 and 7.5.1. Finally, this observational strategy will make it possible to extend the analysis of the gas morphology and ice abundances presented in this section.

7.5 DISCUSSION

Laboratory experiments predict that CH_3OH ice in cold dark clouds and in the coldest regions of protostellar envelopes is desorbed with an efficiency spanning over approximately three orders of magnitude ($10^{-6} - 10^{-3}$ molecules/photon; Öberg *et al.*, 2009b; Bertin *et al.*, 2016; Cruz-Diaz *et al.*, 2016; Martín-Doménech *et al.*, 2016). This range is expected to increase up to $\sim 10^{-2}$ molecules/photon in the disk, as X-rays emitted from the central YSO are likely able to eject CH_3OH molecules from the mid-plane ices (Basalgète *et al.*, 2021a; Basalgète *et al.*, 2021b). The CH_3OH desorption efficiency and by inference the gas-to-ice ratio is highly dependent on the ice structure (crystalline or amorphous) and composition (pure CH_3OH versus CH_3OH mixed with CO molecules), as well as on the temperature, photon energy and flux (e.g., Öberg, 2016). In this study, the laboratory predictions for the CH_3OH gas-to-ice ratio have been tested observationally using literature data. This provides direct observational constraints on the gas-to-ice ratio of CH_3OH in protostellar envelopes, and its dependency on the physical conditions of star-forming regions.

Figure 7.5.1 illustrates the distribution of the CH_3OH gas-to-ice ratios (N_{gas}/N_{ice}) towards low-mass protostars located in three different molecular clouds: Serpens (Chapter 5), Orion (Chapter 6), and Corona Australis. The averaged CH_3OH gas-to-ice ratio (1.2×10^{-4}) determined from millimetric and infrared measurements by Öberg *et al.* (2009a) for Class 0/I sources is over-plotted on this figure as a reference. A detailed comparison between the gas-to-ice ratio determined by Öberg *et al.* (2009a) and the ratios calculated for the sources in the Serpens SVS 4 and the Orion B35A cloud is provided in Chapter 6. In this section we focus on the ratios obtained for Corona Australis and their comparison with the values determined for the two other star-forming regions.

The distribution of CH_3OH gas-to-ice ratios towards the Coronet cluster covers approximately one order of magnitude (i.e., from 1.9×10^{-4} to 1.5×10^{-3}). The uncertainty on the determination of the CH_3OH ice column densities for HH100 IRS1 and IRS7A (Boogert *et al.*, 2008) results in upper limits for their gas-to-ice ratios, consequently we cannot provide solid comparisons for these two sources. In contrast, the values obtained for IRS5A and IRS7B fall in the range of gas-to-ice ratios previously obtained for the protostars located in the Serpens SVS 4 cluster.

The CH_3OH gas-to-ice ratios constrained from gas and ice observations of protostellar envelopes (Figure 7.5.1) do not point to one value but, instead, to a distribution ($\sim10^{-4} - 10^{-3}$) which validates previous laboratory predictions (Öberg *et al.*, 2009b). This distribution agrees with a more complex scenario for the CH_3OH desorption elucidated in the laboratory in which photodissociation (i.e., photo-fragmentation) and recombination processes are triggered during and after the desorption, respectively (e.g., Bertin *et al.*, 2016).

A second interesting observation is that, the CH_3OH gas-to-ice ratios are similar, which suggest that the CH_3OH chemistry at play in cold protostellar envelopes belonging to different low-mass star-forming regions is relatively independent of variations in the physical conditions. A related result came to light when comparing abundances of complex organic molecules observed in distinct star-forming environments (e.g., Galactic disk versus Galactic center, high-mass versus low-mass star-forming region; Jørgensen *et al.*, 2020). A larger sample is however necessary to prove this statement, and additional observations, laboratory experiments and modelling efforts are required to elucidate further the impact of the physical evolution of protostars on their chemical signatures and vice versa.

Our targeted regions (Serpens SVS 4, Orion B35A, and Corona Australis Coronet) share a number of similarities: e.g., they are low-mass star forming regions, they are clustered and finally, they are affected by the presence of outflows and/or Herbig-Haro objects. However, they show distinct physical conditions. For instance, the Serpens SVS 4 cluster is influenced by the presence of the Class 0 binary SMM4 (Pontoppidan *et al.*, 2004), whereas B35A is affected by the nearby high-mass star λ Orionis (Reipurth and Friberg, 2021) and the Coronet is strongly irradiated by the Herbig Ae/Be star R CrA (Lindberg and Jørgensen, 2012). B35A is exposed to an interstellar radiation field χ_{ISRF} of 34 (Wolfire *et al.*, 1989)[2] enhanced by the neighbouring λ Orionis (Dolan and Mathieu, 2002), whereas the radiation field in the

[2]Note that Wolfire *et al.* (1989) report a $\log(G_0)$ of 1.3 which is here converted to χ_{ISRF} by applying the formalism described by Draine and Bertoldi (1996).

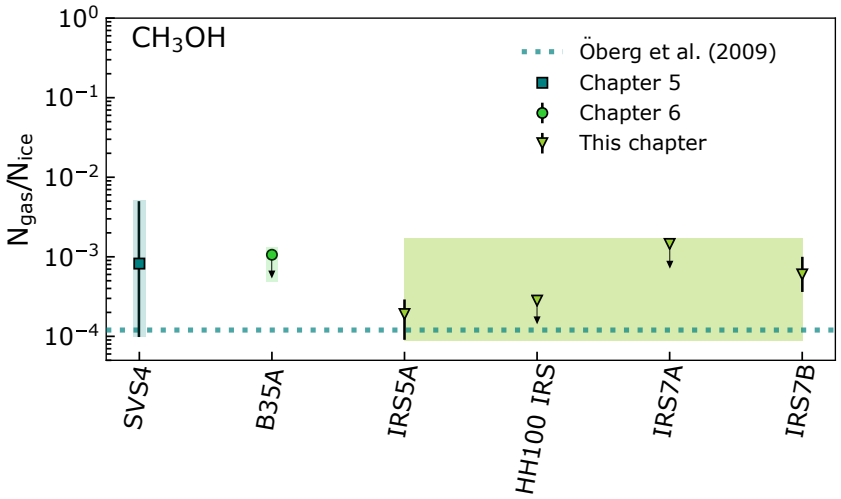

FIGURE 7.5.1: CH_3OH gas-to-ice ratios (N_{gas}/N_{ice}) towards low-mass protostars in the Corona Australis Coronet cluster (triangles). The square and the circle symbolize the averaged CH_3OH gas-to-ice ratios for Serpens SVS 4 and Orion B35A, respectively. The dotted line indicates the reference value by Öberg *et al.* (2009a). The shaded areas indicate the ranges of gas-to-ice ratios towards the three molecular clouds.

Coronet cluster has been estimated to approximately χ_{ISRF} ~750 to account for the high fluxes at millimeter wavelengths (Lindberg and Jørgensen, 2012).

In addition, the molecular clouds in which our targeted regions are located do not share a common formation history. The ongoing low-mass star formation in Serpens Main is a controversial topic in the literature. It might have been triggered by external forcing, possibly cloud-cloud collisions (Duarte-Cabral *et al.*, 2010; Nakamura *et al.*, 2017) or compression from a shock wave from a supernova. However, there is no clear evidence that a nearby supernova ever occurred (Herczeg *et al.*, 2019). Concurrently, it is challenging to explain how cloud–cloud collisions happening at certain locations could propagate over considerable distances without promoting subsequent star-forming collisions ubiquitously in the clouds (Herczeg *et al.*, 2019).

The population of young protostars in the Orion B35A cloud is located in the λ Orionis star-forming region, constituted by a group of massive OB stars surrounded by a ring of dust and gas (Wade, 1957; Murdin and Penston, 1977; Heiles and Habing, 1974; Maddalena and Morris, 1987; Zhang *et al.*, 1989; Lang *et al.*, 2000; Dolan and Mathieu, 2002; Sahan and Haffner, 2016). In contrast to Serpens, the formation of the ring constituting the λ Orionis region is attributed to a supernova explosion occurred roughly 1–6 Myr ago (Dolan and Mathieu, 1999; Dolan and Mathieu, 2002; Kounkel, 2020). The low-mass star formation in B35A was likely triggered by the presence of neighboring massive stars and their stellar winds (Barrado *et al.*, 2018).

Finally, star-formation in Corona Australis has been supposedly promoted by a high-velocity cloud impact onto the Galactic plane (Neuhäuser and Forbrich, 2008). This scenario is based on the study of the three-dimensional motion of the T Tauri stars located in CrA (Neuhäuser *et al.*, 2000). Another possible trigger is the expansion of the Upper Centaurus-Lupus (UCL) su-

perbubble. This hypothesis is based on the finding that CrA is moving away from UCL with 7 km s^{-1} and therefore it was located close to its center about 14 Myr ago (Mamajek *et al.*, 2002).

7.6 CONCLUSIONS

We present 1.3 mm SMA observations towards the Coronet cluster in Corona Australis, a unique astrochemical laboratory to study the effect of external irradiation on the chemical and physical evolution of young protostars. In addition, we make use of multi-wavelengths archival observations (SMA, APEX, Spitzer) to test laboratory predictions for the CH_3OH gas-to-ice ratio in cold protostellar envelopes. Our key findings are:

- In the SMA data we identify eighteen molecular transitions and a total of nine species which include ions (DCO^+), deuterated species (D_2CO) and isotopologues (^{13}CO and $C^{18}O$). The strong UV flux in the region affects the gas-phase chemistry by enhancing the abundance of shocks and photon-dominated regions molecular tracers.

- Luminous H_2CO emission is confined to two bright ridges not associated with the YSOs, in agreement with studies suggesting that the cluster is significantly impacted by external irradiation, plausibly from the Herbig Ae/Be star R CrA.

- Bright and compact SO, SO_2, and SiO emission is observed in the cluster. The SO and SO_2 emissions peak at the IRS7A and SMM1C positions, whereas the SiO feature is located south of R CrA. The distribution of the emission of these tracers suggest that IRS7A, SMM1C, and R CrA are possible driving sources of outflows, jets and Herbig-Haro objects in the region.

- We find a tentative correlation between H_2O ice and CH_3OH gas abundances pointing to a linked chemical behaviour of these two species. We also note a negative trend between NH_4^+ and H_2CO gas abundances, suggesting that the higher temperature regions harbour a lower content of NH_4^+ on the grain surfaces.

- The distribution of CH_3OH gas-to-ice ratios in the Coronet cluster constrained from millimetric and ice observations spans over one order of magnitude (1.9×10^{-4} to 1.5×10^{-3}) and validates previous laboratory predictions by Öberg *et al.* (2009b).

- Similarities are found between CH_3OH gas-to-ice ratios determined in different low-mass star forming regions (Serpens SVS 4 cluster, Orion B35A cloud, and Coronet cluster), characterized by distinct physical conditions and formation histories. This result suggests that the CH_3OH chemistry occurring in cold low-mass envelopes is relatively independent of variations in the physical conditions.

Multiple avenues for future studies can be pursued. Comparisons of gas and ice abundances of key species are currently limited by the low number of infrared surveys. Future infrared facilities such as VLTI-GRAVITY

and JWST will routinely probe pre-stellar cores, proto-stellar envelopes and near edge-on disks, thus significantly increase the number of studied regions. Therefore, it will be feasible to search for gas-ice trends found in other regions, improve our constrains on the CH_3OH gas-to-ice ratios, and ultimately determine ratios for a larger set of interstellar molecules. This approach will provide important feedback on the interactions between ice and gas material during its journey from the molecular cloud to the disk and on the impact of the physical conditions on the physico-chemical evolution of protostars. In this context, the Corona Australis molecular cloud still has much to teach us, hosting one of the youngest population of protostars observed so far.

ACKNOWLEDGEMENTS

This work is based on observations with the Submillimeter Array, Mauna Kea, Hawaii, program code: 2019B-S014. The Submillimeter Array is a joint project between the Smithsonian Astrophysical Observatory and the Academia Sinica Institute of Astronomy and Astrophysics and is funded by the Smithsonian Institution and the Academia Sinica. This publication also makes use of data products from the Wide-field Infrared Survey Explorer, which is a joint project of the University of California, Los Angeles, and the Jet Propulsion Laboratory/California Institute of Technology, funded by the National Aeronautics and Space Administration. JKJ acknowledges the financial support from the European Research Council (ERC) under the European Union's Horizon 2020 research and innovation programme (grant agreement No 646908) through ERC Consolidator Grant "S4F".

Appendix

7.a NON-DETECTIONS

Non-detected transitions in the covered spectral range at the 3σ level are listed in Table 7.A.1, together with their spectroscopic parameters.

TABLE 7.A.1: Non-detected molecular transitions in the SMA data.

Species	Transition	Frequency^a [GHz]	A^a_{ul} [s^{-1}]	E^a_u [K]
CO-species				
p-H_2CO	$11_{2,9}$ – $12_{0,9}$	215.976	3.16×10^{-7}	280
o-H_2CO	$9_{1,8}$ – $9_{1,9}$	216.569	7.24×10^{-6}	68
Deuterated-species				
C_2D^a	$N = 3 - 2$	216.373	3.01×10^{-5}	21
C_2D^b	$N = 3 - 2$	216.428	2.78×10^{-5}	21
HDO	$3_{1,2}$ – $2_{2,1}$	225.897	1.32×10^{-5}	167
N_2D^+	$J = 3 - 2$	231.321	7.08×10^{-4}	22
S-species				
SO	1_2 – 2_1	236.452	1.41×10^{-6}	16
SO_2	$11_{1,11}$ – $10_{0,10}$	221.965	1.15×10^{-4}	60
SO_2	$12_{3,9}$ – $12_{2,10}$	237.069	1.15×10^{-4}	60
^{13}CS	5_5 – 4_4	231.220	2.51×10^{-4}	33
OCS	$J = 18 - 17$	218.903	3.02×10^{-5}	100
OCS	$J = 19 - 18$	231.061	3.55×10^{-5}	111
p-H_2S	$2_{2,0}$ – $2_{1,1}$	216.710	4.90×10^{-4}	84
H_2CS	$7_{1,7}$ – $6_{1,6}$	236.727	1.91×10^{-4}	59
Carbon-chain species				
$^{13}CN^c$	N=2–1	217.265	1.01×10^{-4}	16
$^{13}CN^d$	N=2–1	217.467	1.01×10^{-4}	16
H_2CN	$3_{0,3}$ – $2_{0,2}$	219.852	3.39×10^{-4}	21
HC_3N	$J = 26 - 25$	236.513	1.05×10^{-4}	153
c-C_3H_2	$8_{2,6}$ – $7_{1,7}$	218.448	1.48×10^{-4}	87
c-C_3H_2	$8_{3,6}$ – $7_{2,7}$	218.449	1.48×10^{-4}	87
Other species				
HNCO	$10_{0,10}$ – $9_{0,9}$	219.798	1.48×10^{-4}	58

Notes.^{a} From the Cologne Database for Molecular Spectroscopy (CDMS; Müller *et al.*, 2001) and the Jet Propulsion Laboratory catalog (Pickett *et al.*, 1998). ^{a} $N = 3 - 2$, $J = 7/2 - 5/2$, $F = 5/2 - 3/2$. ^{b} $N = 3 - 2$, $J = 5/2 - 3/2$, $F = 7/2 - 5/2$. ^{c} J=3/2 –1/2. ^{d} J=5/2 –3/2.

Bibliography

1. ALMA Partnership *et al.*, *ApJ* **808**, L3 (2015).
2. K. Acharyya *et al.*, *A&A* **466**, 1005–1012 (2007).
3. C. M. O. D. Alexander *et al.*, *Geochim. Cosmochim. Acta* **71**, 4380–4403 (2007).
4. V. Allen, M. Cordiner, S. Charnley, *arXiv e-prints* (2020).
5. K. Altwegg *et al.*, *Science Advances* **2**, e1600285–e1600285 (2016).
6. F. O. Alves *et al.*, *ApJ* **904**, L6 (2020).
7. J. Alves, M. Lombardi, C. J. Lada, *A&A* **565**, A18 (2014).
8. S. Andersson, E. F. van Dishoeck, *A&A* **491**, 907–916 (2008).
9. S. Andersson *et al.*, *J. Chem. Phys.* **124**, 064715–064715 (2006).
10. D. P. P. Andrade, M. L. M. Rocco, H. M. Boechat-Roberty, *MNRAS* **409**, 1289–1296 (2010).
11. P. André *et al.*, in *Protostars and Planets VI* (Beuther, Henrik et al., 2014), p. 27.
12. P. André *et al.*, *A&A* **518**, L102 (2010).
13. P. André, *Comptes Rendus Geoscience* **349**, 187–197 (2017).
14. P. Andre, D. Ward-Thompson, M. Barsony, *ApJ* **406**, 122 (1993).
15. S. M. Andrews *et al.*, *ApJ* **869**, L41 (2018).
16. M. Ansdell *et al.*, *AJ* **160**, 248 (Dec. 2020).
17. M. Antiñolo *et al.*, *ApJ* **823**, 25 (2016).
18. E. Artur de la Villarmois *et al.*, *A&A* **626**, A71 (2019).
19. C. R. Arumainayagam *et al.*, *Chemical Society Reviews* **48**, 2293–2314 (2019).
20. Y. Aso *et al.*, *ApJ* **863**, 19 (2018).
21. R. Bachiller *et al.*, *A&A* **295**, L51 (1995).
22. R. Bachiller *et al.*, *A&A* **335**, 266–276 (1998).
23. J. Bally, in *Handbook of Star Forming Regions, Volume I* (Reipurth, B., 2008), vol. 4, p. 459.
24. N. Balucani, C. Ceccarelli, V. Taquet, *MNRAS* **449**, L16–L20 (2015).
25. P. J. Barnes *et al.*, *ApJ* **812**, 6 (2015).
26. D. Barrado *et al.*, *A&A* **526**, A21 (2011).
27. D. Barrado *et al.*, *A&A* **612**, A79 (2018).
28. R. Basalgète *et al.*, *A&A* **647**, A35 (2021).
29. R. Basalgète *et al.*, *A&A* **647**, A36 (2021).
30. M. R. Bate, *MNRAS* **475**, 5618–5658 (2018).
31. A. Bayo *et al.*, *A&A* **536**, A63 (2011).
32. C. P. M. Bell *et al.*, *MNRAS* **434**, 806–831 (2013).
33. C. J. Bennett *et al.*, *ApJ* **660**, 1588–1608 (2007).
34. P. J. Benson, P. C. Myers, *ApJS* **71**, 89 (1989).
35. E. A. Bergin, M. Tafalla, *ARA&A* **45**, 339–396 (2007).
36. J. B. Bergner *et al.*, *ApJ* **841**, 120 (2017).
37. J. B. Bergner *et al.*, *ACS Earth and Space Chemistry* **3**, 1564–1575 (2019).
38. M. Bertin *et al.*, *ApJ* **817**, L12 (2016).
39. E. A. Bibo, P. S. The, D. N. Dawanas, *A&A* **260**, 293–302 (1992).
40. S. E. Bisschop *et al.*, *A&A* **449**, 1297–1309 (2006).
41. L. Bizzocchi *et al.*, *A&A* **569**, A27 (2014).

42. P. Bjerkeli *et al.*, *A&A* **546**, A29 (2012).
43. P. Bjerkeli *et al.*, *A&A* **595**, A39 (2016).
44. R. D. Blandford, D. G. Payne, *MNRAS* **199**, 883–903 (1982).
45. S Blanksby, G Ellison, *Accounts of Chemical Research* **36**, 255–263 (2003).
46. J. Blum, G. Wurm, *ARA&A* **46**, 21–56 (2008).
47. D. Bockelee-Morvan *et al.*, *A&A* **287**, 647–665 (1994).
48. C. F. Bohren, D. R. Huffman, *Absorption and scattering of light by small particles* (New York: Wiley, 1983).
49. A. S. Bolina, W. A. Brown, *Surface Science* **598**, 45–56 (2005).
50. W. B. Bonnor, *ZAp* **39**, 143 (1956).
51. S. Bontemps *et al.*, *A&A* **518**, L85 (2010).
52. A. C. A. Boogert, P. A. Gerakines, D. C. B. Whittet, *ARA&A* **53**, 541–581 (2015).
53. A. C. A. Boogert *et al.*, *A&A* **360**, 683–698 (2000).
54. A. C. A. Boogert *et al.*, *ApJ* **678**, 985–1004 (2008).
55. A. C. A. Boogert *et al.*, *ApJ* **729**, 92 (2011).
56. A. C. A. Boogert *et al.*, *ApJ* **777**, 73 (2013).
57. S. Bottinelli *et al.*, *ApJ* **718**, 1100–1117 (2010).
58. F. Brauer, T. Henning, C. P. Dullemond, *A&A* **487**, L1–L4 (2008).
59. D. Bresnahan *et al.*, *A&A* **615**, A125 (2018).
60. D. S. Briggs, F. R. Schwab, R. A. Sramek, in *Synthesis Imaging in Radio Astronomy II* (Taylor, G. B., Carilli, C. L., and Perley, R. A., 1999), vol. 180, p. 127.
61. T. Y. Brooke, K. Sellgren, T. R. Geballe, *ApJ* **517**, 883–900 (1999).
62. A. Brown, *ApJ* **322**, L31 (1987).
63. V. Buch, R. Czerminski, *J. Chem. Phys.* **95**, 6026–6038 (1991).
64. J. V. Buckle *et al.*, *MNRAS* **399**, 1026–1043 (2009).
65. J. V. Buckle *et al.*, *MNRAS* **422**, 521–541 (2012).
66. J. A. Caballero, *A&A* **478**, 667–674 (2008).
67. H. Calcutt *et al.*, *A&A* **616**, A90 (2018).
68. L. Cambrésy, *A&A* **345**, 965–976 (1999).
69. J. A. Cardelli, G. C. Clayton, J. S. Mathis, *ApJ* **345**, 245 (1989).
70. P. Carlhoff *et al.*, *A&A* **560**, A24 (2013).
71. J. M. Carpenter, *AJ* **120**, 3139–3161 (2000).
72. M. M. Casali, C. Eiroa, W. D. Duncan, *A&A* **275**, 195–200 (1993).
73. S. Cazaux *et al.*, *ApJ* **593**, L51–L55 (2003).
74. S. Cazaux *et al.*, *A&A* **585**, A55 (2016).
75. S. Cazaux *et al.*, *ApJ* **849**, 80 (2017).
76. P. Cazzoletti *et al.*, *A&A* **626**, A11 (2019).
77. C. J. Chandler, J. E. Carlstrom, *ApJ* **466**, 338 (1996).
78. N. L. Chapman *et al.*, *ApJ* **690**, 496–511 (2009).
79. S. B. Charnley, A. G. G. M. Tielens, S. D. Rodgers, *ApJ* **482**, L203–L206 (1997).
80. S. B. Charnley, in *IAU Colloq. 161: Astronomical and Biochemical Origins and the Search for Life in the Universe* (Batalli Cosmovici, Cristiano, Bowyer, Stuart, and Werthimer, Dan, 1997), p. 89.
81. H. Chen *et al.*, *ApJ* **445**, 377 (1995).
82. X. Chen, H. G. Arce, *ApJ* **720**, L169–L173 (2010).
83. J. E. Chiar *et al.*, *ApJ* **426**, 240 (1994).
84. J. E. Chiar *et al.*, *ApJ* **570**, 198–209 (2002).
85. J. E. Chiar *et al.*, *ApJ* **731**, 9 (2011).

86. M. Choi, *ApJ* **705**, 1730–1734 (2009).
87. L. E. U. Chu, K. Hodapp, A. Boogert, *ApJ* **904**, 86 (2020).
88. K. J. Chuang *et al.*, *MNRAS* **455**, 1702–1712 (2016).
89. K. J. Chuang *et al.*, *MNRAS* **467**, 2552–2565 (2017).
90. A. Ciaravella *et al.*, *Proceedings of the National Academy of Science* **117**, 16149–16153 (2020).
91. M. P. Collings *et al.*, *ApJ* **583**, 1058–1062 (2003).
92. M. P. Collings *et al.*, *MNRAS* **354**, 1133–1140 (2004).
93. M. S. Connelley, B. Reipurth, A. T. Tokunaga, *AJ* **135**, 2496–2525 (2008).
94. P. S. Conti, E. M. Leep, *ApJ* **193**, 113–124 (1974).
95. A. M. Craigon, http://digitool.lib.strath.ac.uk/R/?func=dbin-jump-full&object_id=27550, PhD thesis, Dept. of Physics, Univ. of Strathclyde, 2015.
96. G. A. Cruz-Diaz *et al.*, *A&A* **592**, A68 (2016).
97. H. M. Cuppen, E. Herbst, *ApJ* **668**, 294–309 (2007).
98. H. M. Cuppen *et al.*, *MNRAS* **417**, 2809–2816 (2011).
99. H. M. Cuppen *et al.*, *Space Sci. Rev.* **212**, 1–58 (2017).
100. A. Dalgarno, in, ed. by B. Bederson, A. Dalgarno (Academic Press, 1994), vol. 32, pp. 57–68.
101. T. M. Dame, P. Thaddeus, *ApJ* **297**, 751–765 (1985).
102. T. M. Dame *et al.*, *ApJ* **322**, 706 (1987).
103. E. Dartois *et al.*, *A&A* **618**, A173 (2018).
104. E. Dartois *et al.*, *Astronomy and Astrophysics* **627**, A55 (2019).
105. E. Dartois *et al.*, *A&A* **634**, A103 (2020).
106. A. Das *et al.*, *ApJS* **237**, 9 (2018).
107. C. J. Davis *et al.*, *MNRAS* **309**, 141–152 (1999).
108. A. Dawes, N. J. Mason, H. J. Fraser, *Phys. Chem. Chem. Phys.* **18**, 1245–1257 (2 2016).
109. C. H. De Vries, G. Narayanan, R. L. Snell, *ApJ* **577**, 798–825 (2002).
110. J. T. Dempsey *et al.*, *MNRAS* **430**, 2534–2544 (2013).
111. J. P. Devlin, *J. Chem. Phys* **96**, 6185–6188 (1992).
112. J. Di Francesco *et al.*, *ApJS* **175**, 277–295 (2008).
113. S. Dib, T. Henning, *A&A* **629**, A135 (2019).
114. O. Dionatos *et al.*, *A&A* **558**, A88 (2013).
115. O. Dionatos *et al.*, *A&A* **563**, A28 (2014).
116. C. J. Dolan, R. D. Mathieu, *AJ* **118**, 2409–2423 (1999).
117. C. J. Dolan, R. D. Mathieu, *AJ* **123**, 387–403 (2002).
118. B. T. Draine, *ARA&A* **41**, 241–289 (2003).
119. B. T. Draine, F. Bertoldi, *ApJ* **468**, 269 (1996).
120. M. N. Drozdovskaya *et al.*, *MNRAS* **490**, 50–79 (2019).
121. A. Duarte-Cabral *et al.*, *A&A* **519**, A27 (2010).
122. F. Dulieu *et al.*, *Scientific Reports* **3**, 1338 (2013).
123. M. M. Dunham *et al.*, in *Protostars and Planets VI* (Beuther, Henrik et al., 2014), p. 195.
124. M. M. Dunham *et al.*, *ApJS* **220**, 11 (2015).
125. R. Dupuy *et al.*, *Nature Astronomy* **2**, 796–801 (2018).
126. A. Duquennoy, M. Mayor, *A&A* **500**, 337–376 (1991).
127. R. Ebert, *ZAp* **37**, 217 (1955).
128. P. Ehrenfreund, S. B. Charnley, *ARA&A* **38**, 427–483 (2000).
129. C. Eiroa, M. M. Casali, *A&A* **223**, L17–L19 (1989).

130. C. Eiroa, A. A. Djupvik, M. M. Casali, in *Handbook of Star Forming Regions, Volume II: The Southern Sky ASP Monograph Publications* (Reipurth, B. ed, 2008), vol. 5, p. 693.
131. C. Eistrup, C. Walsh, E. F. van Dishoeck, *A&A* **595**, A83 (2016).
132. D. D. Eley, E. K. Rideal, *Nature* **146**, 401–402 (1940).
133. I. Evans Neal J. *et al.*, *ApJS* **181**, 321–350 (2009).
134. N. J. Evans II *et al.*, *VizieR Online Data Catalog* **2332** (2014).
135. E. C. Fayolle *et al.*, *ApJ* **739**, L36 (2011).
136. E. C. Fayolle *et al.*, *ApJ* **816**, L28 (2016).
137. G. G. Fazio *et al.*, *ApJS* **154**, 10–17 (2004).
138. G. Fedoseev *et al.*, *MNRAS* **448**, 1288–1297 (2015).
139. G. Fedoseev *et al.*, *MNRAS* **446**, 439–448 (2015).
140. G. Fedoseev *et al.*, *ApJ* **842**, 52 (2017).
141. S. Ferrero *et al.*, *ApJ* **904**, 11 (2020).
142. J. Forbrich, T. Preibisch, *A&A* **475**, 959–972 (2007).
143. J. Forbrich *et al.*, *A&A* **464**, 1003–1013 (2007).
144. D. Foreman-Mackey *et al.*, *PASP* **125**, 306 (2013).
145. H. J. Fraser, E. F. van Dishoeck, *Advances in Space Research* **33**, 14–22 (2004).
146. H. J. Fraser *et al.*, *MNRAS* **327**, 1165–1172 (2001).
147. H. J. Fraser *et al.*, *MNRAS* **353**, 59–68 (2004).
148. S. Frimann, J. K. Jørgensen, T. Haugbølle, *A&A* **587**, A59 (2016).
149. G. W. Fuchs *et al.*, *A&A* **505**, 629–639 (2009).
150. P. A. B. Galli *et al.*, *A&A* **634**, A98 (2020).
151. R. T. Garrod, E. Herbst, *A&A* **457**, 927–936 (2006).
152. R. T. Garrod, V. Wakelam, E. Herbst, *A&A* **467**, 1103–1115 (2007).
153. R. T. Garrod, S. L. Widicus Weaver, E. Herbst, *ApJ* **682**, 283–302 (2008).
154. W. D. Geppert *et al.*, *Faraday Discussions* **133**, 177 (2006).
155. P. A. Gerakines *et al.*, *A&A* **296**, 810 (1995).
156. G. Giardino *et al.*, *A&A* **463**, 275–288 (2007).
157. E. L. Gibb *et al.*, *ApJS* **151**, 35–73 (2004).
158. B. M. Giuliano *et al.*, *A&A* **592**, A81 (2016).
159. P. F. Goldsmith, W. D. Langer, *ApJ* **517**, 209–225 (1999).
160. M. Goto *et al.*, *arXiv e-prints* (2020).
161. R. J. Gould, E. E. Salpeter, *ApJ* **138**, 393 (1963).
162. L. V. Gramajo *et al.*, *AJ* **139**, 2504–2524 (2010).
163. T. Grassi *et al.*, *A&A* **643**, A155 (Nov. 2020).
164. R. O. Gray *et al.*, *AJ* **132**, 161–170 (2006).
165. G. M. Green *et al.*, *ApJ* **810**, 25 (2015).
166. M. J. Griffin *et al.*, *A&A* **518**, L3 (2010).
167. R. J. A. Grim *et al.*, *A&A* **243**, 473 (1991).
168. C. E. Groppi *et al.*, *ApJ* **670**, 489–498 (2007).
169. W. M. Grundy *et al.*, *Science* **367**, aay3705 (2020).
170. R. Güsten *et al.*, *A&A* **454**, L13–L16 (2006).
171. R. A. Gutermuth *et al.*, *ApJ* **673**, L151 (2008).
172. W. Hagen, L. J. Allamandola, J. M. Greenberg, *A&A* **86**, L3–L6 (1980).
173. G. Haro, *ApJ* **115**, 572 (1952).

174. J. Harris, B. Kasemo, *Surface Science* **105**, L281–L287 (1981).
175. D. Harsono *et al.*, *A&A* **562**, A77 (2014).
176. D. Harsono *et al.*, *Nature Astronomy* **2**, 646–651 (2018).
177. P. Hartigan, J. A. Graham, *AJ* **93**, 913 (1987).
178. P. Harvey *et al.*, *ApJ* **663**, 1149–1173 (2007).
179. T. I. Hasegawa, E. Herbst, *MNRAS* **263**, 589 (1993).
180. T. I. Hasegawa, E. Herbst, C. M. Leung, *ApJS* **82**, 167 (1992).
181. T. Hassenkam *et al.*, *Nature* **548**, 78–81 (2017).
182. T. J. Haworth *et al.*, *MNRAS* **501**, 3502–3514 (2021).
183. C. Heiles, H. J. Habing, *A&AS* **14**, 1 (1974).
184. T. T. Helfer *et al.*, *ApJS* **145**, 259–327 (2003).
185. T. Henning, *ARA&A* **48**, 21–46 (2010).
186. T. Henning, G. Meeus, in *Physical Processes in Circumstellar Disks around Young Stars* (Garcia, Paulo J. V., 2011), pp. 114–148.
187. G. H. Herbig, *Vistas in Astronomy* **8**, 109–125 (1966).
188. G. H. Herbig, *ApJ* **111**, 11 (1950).
189. G. H. Herbig, *ApJS* **4**, 337 (1960).
190. E. Herbst, W. Klemperer, *ApJ* **185**, 505–534 (1973).
191. E. Herbst, C. M. Leung, *ApJS* **69**, 271 (1989).
192. E. Herbst, E. F. van Dishoeck, *ARA&A* **47**, 427–480 (2009).
193. G. J. Herczeg *et al.*, *ApJ* **849**, 43 (2017).
194. G. J. Herczeg *et al.*, *ApJ* **878**, 111 (2019).
195. J. Hernández *et al.*, *ApJ* **662**, 1067–1081 (2007).
196. J. Hernández *et al.*, *ApJ* **707**, 705–715 (2009).
197. J. Hernández *et al.*, *ApJ* **794**, 36 (2014).
198. M. Heyer, T. M. Dame, *ARA&A* **53**, 583–629 (2015).
199. C. N. Hinshelwood, in (Oxford University Press, 1940), pp. 36–39.
200. P. T. P. Ho, J. M. Moran, K. Y. Lo, *ApJ* **616**, L1–L6 (2004).
201. S. Hoban *et al.*, *Icarus* **105**, 548–556 (1993).
202. J. A. Högbom, *A&AS* **15**, 417 (1974).
203. D. J. Hollenbach, A. G. G. M. Tielens, *Reviews of Modern Physics* **71**, 173–230 (1999).
204. D. Hollenbach, C. F. McKee, *ApJ* **342**, 306 (1989).
205. D. Hollenbach, E. E. Salpeter, *ApJ* **163**, 155 (1971).
206. M. Honda *et al.*, *ApJ* **690**, L110–L113 (2009).
207. D. M. Hudgins *et al.*, *ApJS* **86**, 713–870 (1993).
208. C. L. H. Hull *et al.*, *ApJ* **847**, 92 (2017).
209. R. L. Hurt, M. Barsony, *ApJ* **460**, L45 (1996).
210. S. Ioppolo *et al.*, *ApJ* **686**, 1474–1479 (2008).
211. S. Ioppolo *et al.*, *MNRAS* **413**, 2281–2287 (2011).
212. S. Ioppolo *et al.*, *A&A* **646**, A172 (2021).
213. M. Ishii *et al.*, *AJ* **124**, 2790–2798 (2002).
214. J. H. Jeans, *Philosophical Transactions of the Royal Society of London Series A* **199**, 1–53 (1902).
215. R. D. Jeffries, *MNRAS* **376**, 1109–1119 (2007).
216. A. Jiménez-Escobar *et al.*, *ApJ* **820**, 25 (2016).
217. A. Jiménez-Escobar *et al.*, *ApJ* **868**, 73 (2018).

218. I. Jiménez-Serra *et al.*, *A&A* **482**, 549–559 (2008).
219. I. Jiménez-Serra *et al.*, *Astrobiology* **20**, 1048–1066 (2020).
220. D. Johnstone *et al.*, *ApJ* **559**, 307–317 (2001).
221. J. K. Jørgensen *et al.*, *A&A* **415**, 1021–1037 (2004).
222. J. K. Jørgensen *et al.*, *A&A* **595**, A117 (2016).
223. J. K. Jørgensen, A. Belloche, R. T. Garrod, *ARA&A* **58**, 727–778 (2020).
224. G. Jungclaus *et al.*, *Meteoritics* **11**, 231–237 (1976).
225. J. Kauffmann *et al.*, *A&A* **487**, 993–1017 (2008).
226. J. V. Keane *et al.*, *A&A* **376**, 254–270 (2001).
227. M. Keppler *et al.*, *A&A* **617**, A44 (2018).
228. G. Kim *et al.*, *ApJS* **249**, 33 (2020).
229. R. F. Knacke *et al.*, *ApJ* **179**, 847–854 (1973).
230. C. Knez *et al.*, *ApJ* **635**, L145–L148 (2005).
231. J. Koda *et al.*, *ApJS* **193**, 19 (2011).
232. K. W. Kolasinski, in (Wiley, J. & Sons Ltd., Chichester, England, 1st Ed., 2002).
233. V. Könyves *et al.*, *A&A* **584**, A91 (2015).
234. M. Kounkel, *ApJ* **902**, 122 (2020).
235. M. Kounkel *et al.*, *AJ* **156**, 84 (2018).
236. L. E. Kristensen, M. M. Dunham, *A&A* **618**, A158 (2018).
237. L. E. Kristensen *et al.*, *A&A* **516**, A57 (2010).
238. M. Kuffmeier, B. Zhao, P. Caselli, *A&A* **639**, A86 (2020).
239. M. Kuffmeier, T. Haugbølle, Å. Nordlund, *ApJ* **846**, 7 (2017).
240. Y. Kurono, K.-I. Morita, T. Kamazaki, *PASJ* **61**, 873 (2009).
241. C. J. Lada, J. H. Black, *ApJ* **203**, L75–L79 (1976).
242. C. J. Lada, in *Star Forming Regions* (Peimbert, Manuel and Jugaku, Jun, 1987), vol. 115, p. 1.
243. E. F. Ladd, G. A. Fuller, J. R. Deane, *ApJ* **495**, 871–890 (1998).
244. W. J. Lang *et al.*, *A&A* **357**, 1001–1012 (2000).
245. P. Langevin, *J. Phys. Theor. Appl.* **4**, 678 (1905).
246. I. Langmuir, *Trans. Faraday Soc.* **17**, 607–620 (1922).
247. B. Larsson *et al.*, *A&A* **363**, 253–268 (2000).
248. L. Le Roy *et al.*, *A&A* **583**, A1 (2015).
249. H. H. Lee *et al.*, *A&A* **311**, 690–707 (1996).
250. H.-T. Lee *et al.*, *ApJ* **624**, 808–820 (2005).
251. K. I. Lee *et al.*, *ApJ* **797**, 76 (2014).
252. K. Levenberg, *Quart. Appl. Math.* **2**, 164–168 (1944).
253. Y. Lin *et al.*, *ApJ* **840**, 22 (2017).
254. J. E. Lindberg, J. K. Jørgensen, *A&A* **548**, A24 (2012).
255. J. E. Lindberg *et al.*, *A&A* **584**, A28 (2015).
256. J. E. Lindberg *et al.*, *A&A* **566**, A74 (2014).
257. J. E. Lindberg *et al.*, *ApJ* **835**, 3 (2017).
258. H. Linnartz, S. Ioppolo, G. Fedoseev, *International Reviews in Physical Chemistry* **34**, 205–237 (2015).
259. T. Liu *et al.*, *ApJS* **222**, 7 (2016).
260. R. Lüst, A. Schlüter, *ZAp* **38**, 190 (1955).
261. M.-M. Mac Low, R. S. Klessen, *Reviews of Modern Physics* **76**, 125–194 (2004).
262. R. J. Maddalena, M. Morris, *ApJ* **323**, 179 (1987).

263. E. E. Mamajek, in *Exoplanets and Disks: Their Formation and Diversity* (Usuda, Tomonori, Tamura, Motohide, and Ishii, Miki, 2009), vol. 1158, pp. 3–10.

264. E. E. Mamajek, M. R. Meyer, J. Liebert, *AJ* **124**, 1670–1694 (2002).

265. S. Manigand *et al.*, *A&A* **635**, A48 (2020).

266. D. Marquardt, *J. Soc. Indust. Appl. Math.* **11**, 431–441 (1963).

267. R. Martín-Doménech, G. M. Muñoz Caro, G. A. Cruz-Díaz, *A&A* **589**, A107 (2016).

268. R. Martín-Doménech *et al.*, *ApJ* **880**, 130 (2019).

269. R. D. Mathieu, in *in Handbook of Star Forming Regions, Volume I. The Northern Sky* (Reipurth, B. ed, 2008), vol. 4, ASP Monographs, p. 757.

270. A. J. Maury *et al.*, *A&A* **621**, A76 (2019).

271. B. A. McGuire, *ApJS* **239**, 17 (2018).

272. J. P. McMullin *et al.*, in *Astronomical Data Analysis Software and Systems XVI* (Shaw, R. A., Hill, F., and Bell, D. J., 2007), vol. 376, p. 127.

273. J. P. McMullin *et al.*, *ApJ* **424**, 222 (1994).

274. J. P. McMullin *et al.*, *ApJ* **536**, 845–856 (2000).

275. S. T. Megeath *et al.*, *AJ* **144**, 192 (2012).

276. S. T. Megeath *et al.*, *AJ* **151**, 5 (2016).

277. C. Meinert *et al.*, *Science* **352**, 208–212 (2016).

278. K. M. Menten *et al.*, *A&A* **474**, 515–520 (2007).

279. D. Mesa *et al.*, *A&A* **624**, A4 (2019).

280. L. Mestel, *MNRAS* **138**, 359 (1968).

281. O. Miettinen *et al.*, *A&A* **486**, 799–806 (2008).

282. M. Minissale *et al.*, *A&A* **585**, A24 (2016).

283. M. Minissale *et al.*, *MNRAS* **458**, 2953–2961 (2016).

284. N. Miyauchi *et al.*, *Chemical Physics Letters* **456**, 27–30 (2008).

285. P. Modica, M. E. Palumbo, G. Strazzulla, *Planet. Space Sci.* **73**, 425–429 (2012).

286. S. J. Mojzsis *et al.*, *Nature* **384**, 55–59 (1996).

287. L. K. Morgan *et al.*, *A&A* **477**, 557–571 (2008).

288. J. C. Mottram *et al.*, *A&A* **600**, A99 (2017).

289. J. Moultaka *et al.*, *A&A* **425**, 529–542 (2004).

290. G. M. Muñoz Caro *et al.*, *ACS Earth and Space Chemistry* **3**, 2138–2157 (2019).

291. H. S. P. Müller *et al.*, *A&A* **370**, L49–L52 (2001).

292. M. J. Mumma, S. B. Charnley, *ARA&A* **49**, 471–524 (2011).

293. K. Murakawa, M. Tamura, T. Nagata, *ApJS* **128**, 603–613 (2000).

294. P. Murdin, M. V. Penston, *MNRAS* **181**, 657 (1977).

295. N. M. Murillo *et al.*, *A&A* **592**, A56 (2016).

296. P. C. Myers, E. F. Ladd, *ApJ* **413**, L47 (1993).

297. P. C. Myers, R. A. Linke, P. J. Benson, *ApJ* **264**, 517–537 (1983).

298. P. C. Myers *et al.*, *ApJ* **324**, 907 (1988).

299. P. C. Myers, *ApJ* **700**, 1609–1625 (2009).

300. F. Nakamura *et al.*, *ApJ* **837**, 154 (2017).

301. J. Nelder, R. Mead, *The Computer Journal* **7**, 308 (1965).

302. D. A. Neufeld, A. Dalgarno, *ApJ* **340**, 869 (1989).

303. R. Neuhäuser, J. Forbrich, in *Handbook of Star Forming Regions, Volume II* (Reipurth, B., 2008), vol. 5, p. 735.

304. R. Neuhäuser *et al.*, *A&AS* **146**, 323–347 (2000).

305. B. Nisini *et al.*, *A&A* **518**, L120 (2010).

306. J. A. Noble *et al.*, *MNRAS* **421**, 768–779 (2012).
307. J. A. Noble *et al.*, *ApJ* **775**, 85 (2013).
308. J. A. Noble *et al.*, *Monthly Notices of the Royal Astronomical Society* **467**, 4753–4762 (2017).
309. J. A. Noble, PhD thesis, Dept. of Physics, Univ. of Strathclyde, 2011.
310. M. Nuevo, G. Cooper, S. A. Sandford, *Nature Communications* **9**, 5276 (2018).
311. D. J. Nutter, D. Ward-Thompson, P. André, *MNRAS* **357**, 975–982 (2005).
312. K. I. Öberg, S. Bottinelli, E. F. van Dishoeck, *A&A* **494**, L13–L16 (2009).
313. K. I. Öberg *et al.*, *ApJ* **621**, L33–L36 (2005).
314. K. I. Öberg *et al.*, *A&A* **504**, 891–913 (2009).
315. K. I. Öberg *et al.*, *ApJ* **740**, 109 (2011).
316. K. I. Öberg, *Chemical Reviews* **116**, 9631–9663 (2016).
317. K. I. Öberg, E. A. Bergin, *Phys. Rep.* **893**, 1–48 (2021).
318. K. I. Öberg, R. Murray-Clay, E. A. Bergin, *ApJ* **743**, L16 (2011).
319. K. I. Öberg *et al.*, *ApJ* **740**, 14 (2011).
320. T. Oka, *Proceedings of the National Academy of Science* **103**, 12235–12242 (2006).
321. G. N. Ortiz-León *et al.*, *ApJ* **869**, L33 (2018).
322. V. Ossenkopf, T. Henning, *A&A* **291**, 943–959 (1994).
323. P. Padoan, Å. Nordlund, *ApJ* **576**, 870–879 (2002).
324. Y. J. Pendleton, A. G. G. M. Tielens, M. W. Werner, *ApJ* **349**, 107 (1990).
325. E. M. Penteado, C. Walsh, H. M. Cuppen, *ApJ* **844**, 71 (2017).
326. G. Perotti *et al.*, *A&A* **643**, A48 (2020).
327. G. Perotti *et al.*, *A&A* **650**, A168 (2021).
328. D. E. Peterson *et al.*, *ApJS* **194**, 43 (2011).
329. H. M. Pickett *et al.*, *J. Quant. Spectr. Rad. Transf.* **60**, 883–890 (1998).
330. J. B. Pickles, D. A. Williams, *Ap&SS* **52**, 443–452 (1977).
331. M. Planck, *Verhandl. Dtsch. phys. Ges.* **2**, 202 (1900).
332. D. Polychroni *et al.*, *ApJ* **777**, L33 (2013).
333. K. M. Pontoppidan, *A&A* **453**, L47–L50 (2006).
334. K. M. Pontoppidan, S. M. Blevins, *Faraday Discussions* **168**, 49–60 (2014).
335. K. M. Pontoppidan, E. F. van Dishoeck, E. Dartois, *A&A* **426**, 925–940 (2004).
336. K. M. Pontoppidan *et al.*, *A&A* **408**, 981–1007 (2003).
337. K. M. Pontoppidan *et al.*, *A&A* **404**, L17–L20 (2003).
338. K. M. Pontoppidan *et al.*, *ApJ* **678**, 1005–1031 (2008).
339. K. M. Pontoppidan *et al.*, in *Protostars and Planets VI* (Beuther, Henrik et al., 2014), p. 363.
340. K. M. Pontoppidan *et al.*, *ApJ* **874**, 92 (2019).
341. M. S. Povich *et al.*, *ApJS* **209**, 31 (2013).
342. T. Preibisch, *A&A* **410**, 951–959 (2003).
343. T. Preibisch, *A&A* **428**, 569–577 (2004).
344. R. E. Pudritz, T. P. Ray, *Frontiers in Astronomy and Space Sciences* **6**, 54 (2019).
345. D. Qasim *et al.*, *A&A* **612**, A83 (2018).
346. D. Qasim *et al.*, *Nature Astronomy* **4**, 781–785 (2020).
347. S.-L. Qin, Y.-F. Wu, *Chinese J. Astron. Astrophys.* **3**, 69–74 (2003).
348. D. Rabli, D. R. Flower, *MNRAS* **406**, 95–101 (2010).
349. F. R. S. Rayleigh, *XXXI. Investigations in optics, with special reference to the spectroscope*, 1879.
350. P. Redondo, C. Barrientos, A. Largo, *ApJ* **836**, 240 (2017).

351. P. Redondo *et al.*, *A&A* **603**, A139 (2017).
352. B. Reipurth, *VizieR Online Data Catalog*, V/104 (2000).
353. B. Reipurth, J. Bally, *ARA&A* **39**, 403–455 (2001).
354. B. Reipurth, P. Friberg, *MNRAS* **501**, 5938–5947 (2021).
355. V. M. Rivilla *et al.*, *MNRAS* **483**, L114–L119 (2019).
356. H. Roberts, T. J. Millar, *A&A* **361**, 388–398 (2000).
357. T. P. Robitaille, *A&A* **600**, A11 (2017).
358. T. P. Robitaille *et al.*, *ApJS* **169**, 328–352 (2007).
359. T. P. Robitaille *et al.*, *ApJS* **167**, 256–285 (2006).
360. W. R. M. Rocha, S. Pilling, *ApJ* **803**, 18 (2015).
361. K. Rohlfs, T. L. Wilson, *Tools of Radio Astronomy* (Springer Verlag, 1996).
362. G. S. Rossano, *AJ* **83**, 234–240 (1978).
363. L. S. Rothman *et al.*, *Appl. Opt.* **26**, 4058–4097 (1987).
364. M. Rubin *et al.*, *MNRAS* **489**, 594–607 (2019).
365. D. P. Ruffle, E. Herbst, *MNRAS* **322**, 770–778 (2001).
366. D. P. Ruffle, E. Herbst, *MNRAS* **324**, 1054–1062 (2001).
367. D. Rumble *et al.*, *MNRAS* **448**, 1551–1573 (2015).
368. M. Sahan, L. M. Haffner, *AJ* **151**, 147 (2016).
369. G. Santangelo *et al.*, *A&A* **538**, A45 (2012).
370. S. L. Schnee *et al.*, *ApJ* **634**, 442–450 (2005).
371. S. Schneider, B. G. Elmegreen, *ApJS* **41**, 87–95 (1979).
372. F. L. Schöier *et al.*, *A&A* **390**, 1001–1021 (2002).
373. F. L. Schöier *et al.*, *A&A* **432**, 369–379 (2005).
374. F. L. Schöier *et al.*, *A&A* **454**, L67–L70 (2006).
375. W. A. Schutte *et al.*, *A&A* **343**, 966–976 (1999).
376. D. M. Segura-Cox *et al.*, *ApJ* **866**, 161 (2018).
377. D. M. Segura-Cox *et al.*, *Nature* **586**, 228–231 (2020).
378. R. J. Shannon *et al.*, *Nature Chemistry* **5**, 745–749 (2013).
379. R. J. Shannon *et al.*, *RSC Advances* **4**, 26342–26353 (2014).
380. S. Sharpless, *ApJS* **4**, 257 (1959).
381. T. Shimonishi *et al.*, *ApJ* **855**, 27 (2018).
382. F. H. Shu, *ApJ* **214**, 488–497 (1977).
383. M. A. J. Simons, T. Lamberts, H. M. Cuppen, *A&A* **634**, A52 (2020).
384. D. Skouteris *et al.*, *ApJ* **854**, 135 (2018).
385. M. F. Skrutskie *et al.*, *AJ* **131**, 1163–1183 (2006).
386. L. Song, J. Kästner, *ApJ* **850**, 118 (2017).
387. S. Spezzano *et al.*, *A&A* **643**, A60 (2020).
388. F. Stahler, S. W. Palla, in *The Formation of Stars* (Wiley-VCH Verlag GmbG & Co, 2004).
389. S. Stanimirovic, in *Single-Dish Radio Astronomy: Techniques and Applications* (Stanimirovic, Snezana et al., 2002), vol. 278, pp. 375–396.
390. T. P. Stecher, D. A. Williams, *Astrophys. Lett.* **4**, 99 (1969).
391. D. P. Stevenson, D. O. Schissler, *J. Chem. Phys.* **29**, 282 (1958).
392. S. E. Strom, G. L. Grasdalen, K. M. Strom, *ApJ* **191**, 111–142 (1974).
393. K. Sugitani, Y. Fukui, K. Ogura, *ApJS* **77**, 59 (1991).
394. A. N. Suutarinen *et al.*, *MNRAS* **440**, 1844–1855 (2014).

395. A. Suutarinen, http://oro.open.ac.uk/61309/, PhD thesis, Dept. of Physics, The Open University, 2015.
396. A. Suutarinen, *omnifit v0.1*, https://doi.org/10.5281/zenodo.29354, 2015.
397. K. N. R. Taylor, J. W. V. Storey, *MNRAS* **209**, 5P–10 (1984).
398. S. Terebey, F. H. Shu, P. Cassen, *ApJ* **286**, 529–551 (1984).
399. J. Terwisscha van Scheltinga *et al.*, *A&A* **611**, A35 (2018).
400. W.-F. Thi *et al.*, *A&A* **449**, 251–265 (2006).
401. A. G. G. M. Tielens, W. Hagen, *A&A* **114**, 245–260 (1982).
402. J. J. Tobin *et al.*, *Nature* **492**, 83–85 (2012).
403. J. J. Tobin *et al.*, *ApJ* **805**, 125 (2015).
404. W. Tscharnuter, *A&A* **39**, 207 (1975).
405. B. E. Turner, *ApJ* **501**, 731–748 (1998).
406. Ł. Tychoniec *et al.*, *A&A* **632**, A101 (2019).
407. Ł. Tychoniec *et al.*, *A&A* **640**, A19 (2020).
408. M. Vasta *et al.*, *A&A* **537**, A98 (2012).
409. A. I. Vasyunin, E. Herbst, *ApJ* **769**, 34 (2013).
410. A. I. Vasyunin *et al.*, *ApJ* **842**, 33 (2017).
411. F. Vazart *et al.*, *MNRAS* **499**, 5547–5561 (2020).
412. R. Visser, S. D. Doty, E. F. van Dishoeck, *A&A* **534**, A132 (2011).
413. R. Visser *et al.*, *A&A* **495**, 881–897 (2009).
414. S. N. Vogel *et al.*, *ApJ* **283**, 655–667 (1984).
415. C. M. Wade, *AJ* **62**, 148 (1957).
416. A. F. Wagner, M. M. Graff, *ApJ* **317**, 423 (1987).
417. V. Wakelam *et al.*, *Molecular Astrophysics* **9**, 1–36 (2017).
418. C. Walsh *et al.*, *ApJ* **823**, L10 (2016).
419. F. M. Walter *et al.*, *Mem. Soc. Astron. Italiana* **68**, 1081–1088 (1997).
420. H. Wang *et al.*, *ApJ* **617**, 1191–1203 (2004).
421. N. Watanabe, A. Kouchi, *ApJ* **571**, L173–L176 (2002).
422. Y. Watanabe *et al.*, *ApJ* **745**, 126 (2012).
423. W. D. Watson, E. E. Salpeter, *ApJ* **174**, 321 (1972).
424. W. D. Watson, *ApJ* **183**, L17 (1973).
425. J. C. Weingartner, B. T. Draine, *ApJ* **548**, 296–309 (2001).
426. A. Weiß *et al.*, *A&A* **365**, 571–587 (2001).
427. M. S. Westley *et al.*, *Nature* **373**, 405–407 (1995).
428. G. J. White, M. M. Casali, C. Eiroa, *A&A* **298**, 594 (1995).
429. B. A. Whitney *et al.*, *ApJ* **598**, 1079–1099 (2003).
430. D. C. B. Whittet *et al.*, *ApJ* **742**, 28 (2011).
431. D. A. Williams, S. Viti, *Observational Molecular Astronomy: Exploring the Universe Using Molecular Line Emissions* (Cambridge University Press, 2013).
432. J. P. Williams, W. M. J. Best, *ApJ* **788**, 59 (2014).
433. J. P. Williams, L. A. Cieza, *ARA&A* **49**, 67–117 (2011).
434. T. L. Wilson, *Reports on Progress in Physics* **62**, 143–185 (1999).
435. T. L. Wilson, F. Matteucci, *A&A Rev.* **4**, 1–33 (1992).
436. A. J. Winter *et al.*, *MNRAS* **491**, 903–922 (2020).
437. M. G. Wolfire, D. Hollenbach, A. G. G. M. Tielens, *ApJ* **344**, 770 (1989).
438. E. L. Wright *et al.*, *AJ* **140**, 1868–1881 (2010).

439. B. Yang *et al.*, *ApJ* **718**, 1062–1069 (2010).
440. H.-W. Yi *et al.*, *ApJS* **236**, 51 (2018).
441. H.-W. Yi *et al.*, *arXiv e-prints*, arXiv:2103.03499 (2021).
442. L. Zamirri *et al.*, *MNRAS* **480**, 1427–1444 (2018).
443. G. Zasowski *et al.*, *ApJ* **694**, 459–478 (2009).
444. F. Zernike, *Physica* **5**, 785–795 (1938).
445. C. Y. Zhang *et al.*, *A&A* **218**, 231–240 (1989).
446. C. Zhang *et al.*, *MNRAS* **497**, 793–808 (2020).
447. Z.-Y. Zhang *et al.*, *Nature* **558**, 260–263 (2018).
448. C. Zucker *et al.*, *ApJ* **879**, 125 (2019).
449. C. Zucker *et al.*, *A&A* **633**, A51 (2020).
450. P. H. van Cittert, *Physica* **1**, 201–210 (1934).
451. E. F. van Dishoeck, in *Millimetre and Submillimetre Astronomy* (Wolstencroft, R. D. and Burton, W. B., 1988), vol. 147, p. 117.
452. E. F. van Dishoeck, J. H. Black, *ApJS* **62**, 109 (1986).
453. E. F. van Dishoeck, E. A. Bergin, *arXiv e-prints* (2020).
454. E. F. van Dishoeck, J. H. Black, *ApJ* **334**, 771 (1988).
455. E. F. van Dishoeck, G. A. Blake, *ARA&A* **36**, 317–368 (1998).
456. M. L. van Gelder *et al.*, *A&A* **639**, A87 (2020).
457. S. E. van Terwisga *et al.*, *A&A* **640**, A27 (2020).
458. H. C. van de Hulst, *Recherches Astronomiques de l'Observatoire d'Utrecht* **11**, 2.i–2 (1946).
459. M. L. R. van 't Hoff *et al.*, *A&A* **599**, A101 (2017).
460. M. L. R. van 't Hoff *et al.*, *ApJ* **864**, L23 (2018).